



OGLE-2018-BLG-1185b: A Low-mass Microlensing Planet Orbiting a Low-mass Dwarf

Iona Kondo^{1,64} , Jennifer C. Yee^{2,65,67} , David P. Bennett^{3,4} , Takahiro Sumi¹ , Naoki Koshimoto⁵ , Ian A. Bond⁶,
Andrew Gould^{7,8}, Andrzej Udalski^{9,68} , Yossi Shvartzvald¹⁰ , Youn Kil Jung^{11,12} , Weicheng Zang¹³ ,
Valerio Bozza^{14,15,69} , Etienne Bachelet^{16,69} , Markus P. G. Hundertmark^{17,69} , Nicholas J. Rattenbury¹⁸

(Leading Authors),

F. Abe¹⁹, R. Barry³ , A. Bhattacharya^{3,4}, M. Donachie¹⁸, A. Fukui^{20,21} , H. Fujii¹⁹, Y. Hirao¹, S. Ishitani Silva^{3,22}, Y. Itow¹⁹ ,
R. Kirikawa¹, M. C. A. Li¹⁸, Y. Matsubara¹⁹, S. Miyazaki¹ , Y. Muraki¹⁹ , G. Olmschenk³ , C. Ranc²³ , Y. Satoh¹, H. Shoji¹,
D. Suzuki¹, Y. Tanaka¹, P. J. Tristram²⁴, T. Yamawaki¹, A. Yonehara²⁵

(The MOA Collaboration),

P. Mróz²⁶ , R. Poleski⁹ , J. Skowron⁹ , M. K. Szymański⁹ , I. Soszyński⁹ , S. Kozłowski⁹ , P. Pietrukowicz⁹ ,
K. Ulaczyk^{9,27} , K. A. Rybicki⁹, P. Iwanek⁹ , M. Wrona⁹

(The OGLE Collaboration),

M. D. Albrow²⁸ , S.-J. Chung^{11,12}, C. Han²⁹ , K.-H. Hwang¹¹ , H.-W. Kim¹¹, I.-G. Shin¹¹ , S.-M. Cha^{11,30}, D.-J. Kim¹¹,
S.-L. Kim^{11,12}, C.-U. Lee¹¹, D.-J. Lee¹¹, Y. Lee^{11,30}, B.-G. Park^{11,12}, R. W. Pogge⁸, Y.-H. Ryu¹¹

(The KMTNet Collaboration),

C. A. Beichman³¹, G. Bryden³² , S. Calchi Novati³¹, S. Carey³¹ , B. S. Gaudi⁸ , C. B. Henderson³¹ , W. Zhu³³

(The Spitzer Team),

D. Maoz³⁴ , M. T. Penny³⁵

(The LCO Follow-up Team),

M. Dominik³⁶, U. G. Jørgensen³⁷ , P. Longa-Peña³⁸, N. Peixinho³⁹ , S. Sajadian⁴⁰ , J. Skottfelt⁴¹, C. Snodgrass⁴² ,
J. Tregloan-Reed⁴³, M. J. Burgdorf⁴⁴, J. Campbell-White⁴⁵, S. Dib^{7,37}, Y. I. Fujii^{37,46,47,48,49}, T. C. Hinse^{50,51}, E. Khalouei⁵² ,
S. Rahvar⁵² , M. Rabus^{53,54} , J. Southworth⁵⁵

(The MiNDSTeP Collaboration),

and

Y. Tsapras⁵⁶, R. A. Street⁵⁶ , D. M. Bramich^{57,58,59}, A. Cassan⁶⁰, K. Horne⁶¹ , J. Wambsganss⁵⁶ , S. Mao⁶², and A. Saha⁶³

(The ROME/REA Project Team)

¹ Department of Earth and Space Science, Graduate School of Science, Osaka University, Toyonaka, Osaka 560-0043, Japan

² Center for Astrophysics | Harvard & Smithsonian, 60 Garden Street, Cambridge, MA 02138, USA

³ Code 667, NASA Goddard Space Flight Center, Greenbelt, MD 20771, USA

⁴ Department of Astronomy, University of Maryland, College Park, MD 20742, USA

⁵ Department of Astronomy, Graduate School of Science, The University of Tokyo, 7-3-1 Hongo, Bunkyo-ku, Tokyo 113-0033, Japan

⁶ Institute of Natural and Mathematical Sciences, Massey University, Auckland 0745, New Zealand

⁷ Max Planck Institute for Astronomy, Königstuhl 17, D-69117, Heidelberg, Germany

⁸ Department of Astronomy, Ohio State University, 140 W. 18th Avenue, Columbus, OH 43210, USA

⁹ Warsaw University Observatory, Al. Ujazdowskie 4, 00-478 Warszawa, Poland

¹⁰ Department of Particle Physics and Astrophysics, Weizmann Institute of Science, Rehovot 76100, Israel

¹¹ Korea Astronomy and Space Science Institute, Daejeon 34055, Republic of Korea

¹² University of Science and Technology, Korea, (UST), 217 Gajeong-ro Yuseong-gu, Daejeon 34113, Republic of Korea

¹³ Department of Astronomy, Tsinghua University, Beijing 100084, People's Republic of China

¹⁴ Dipartimento di Fisica "E.R. Caianiello," Università di Salerno, Via Giovanni Paolo II 132, I-84084, Fisciano, Italy

¹⁵ Istituto Nazionale di Fisica Nucleare, Sezione di Napoli, Napoli, Italy

¹⁶ Las Cumbres Observatory, 6740 Cortona Dr., Ste. 102, 93117 Goleta, CA, USA

¹⁷ Astronomisches Rechen-Institut, Zentrum für Astronomie der Universität Heidelberg (ZAH), D-69120 Heidelberg, Germany

¹⁸ Department of Physics, University of Auckland, Private Bag 92019, Auckland, New Zealand

¹⁹ Institute for Space-Earth Environmental Research, Nagoya University, Nagoya 464-8601, Japan

²⁰ Department of Earth and Planetary Science, Graduate School of Science, The University of Tokyo, 7-3-1 Hongo, Bunkyo-ku, Tokyo 113-0033, Japan

²¹ Instituto de Astrofísica de Canarias, Vía Láctea s/n, E-38205 La Laguna, Tenerife, Spain

²² Department of Physics, The Catholic University of America, Washington, DC 20064, USA

²³ Sorbonne Université, CNRS, UMR 7095, Institut d'Astrophysique de Paris, 98 bis bd Arago, F-75014 Paris, France

²⁴ University of Canterbury Mt. John Observatory, P.O. Box 56, Lake Tekapo 8770, New Zealand

²⁵ Department of Physics, Faculty of Science, Kyoto Sangyo University, 603-8555 Kyoto, Japan

²⁶ Division of Physics, Mathematics, and Astronomy, California Institute of Technology, Pasadena, CA 91125, USA

²⁷ Department of Physics, University of Warwick, Gibbet Hill Road, Coventry, CV4 7AL, UK

²⁸ University of Canterbury, Department of Physics and Astronomy, Private Bag 4800, Christchurch 8020, New Zealand

²⁹ Department of Physics, Chungbuk National University, Cheongju 28644, Republic of Korea

³⁰ School of Space Research, Kyung Hee University, Yongin, Gyeonggi 17104, Republic of Korea

³¹ Infrared Processing and Analysis Center, Mail Code 100-22, California Institute of Technology, 1200 E. California Boulevard, Pasadena, CA 91125, USA

³² Jet Propulsion Laboratory, California Institute of Technology, 4800 Oak Grove Drive, Pasadena, CA 91109, USA

³³ Canadian Institute for Theoretical Astrophysics, University of Toronto, 60 St. George Street, Toronto, ON M5S 3H8, Canada

³⁴ School of Physics and Astronomy, Tel-Aviv University, Tel-Aviv 6997801, Israel

³⁵ Department of Physics & Astronomy, Louisiana State University, Baton Rouge, LA 70803-4001, USA

³⁶ University of St. Andrews, Centre for Exoplanet Science, SUPA School of Physics & Astronomy, North Haugh, St. Andrews, KY16 9SS, UK

³⁷ Centre for ExoLife Sciences, Niels Bohr Institute, University of Copenhagen, Øster Voldgade 5, DK-1350, Copenhagen, Denmark

³⁸ Centro de Astronomía (CITEVA), Universidad de Antofagasta, Avda. U. de Antofagasta 02800, Antofagasta, Chile³⁹ Instituto de Astrofísica e Ciências do Espaço, Universidade de Coimbra, PT3040-004 Coimbra, Portugal⁴⁰ Department of Physics, Isfahan University of Technology, Isfahan, Iran⁴¹ Centre for Electronic Imaging, Department of Physical Sciences, The Open University, Milton Keynes, MK7 6AA, UK⁴² Institute for Astronomy, University of Edinburgh, Royal Observatory, Edinburgh EH9 3HJ, UK⁴³ Instituto de Investigación en Astronomía y Ciencias Planetarias, Universidad de Atacama, Copiapó, Atacama, Chile⁴⁴ Universität Hamburg, Faculty of Mathematics, Informatics, and Natural Sciences, Department of Earth Sciences, Meteorological Institute, Bundesstraße 55, D-20146 Hamburg, Germany⁴⁵ SUPA, School of Science and Engineering, University of Dundee, Nethergate, Dundee DD1 4HN, UK⁴⁶ Institute for Advanced Research, Nagoya University, Furo-cho, Chikusa-ku, Nagoya 464-8601, Japan⁴⁷ Department of Physics, Nagoya University, Furo-cho, Chikusa-ku, Nagoya 464-8602, Japan⁴⁸ Niels Bohr Institute & Centre for Star and Planet Formation, University of Copenhagen, Øster Voldgade 5, DK-1350, Copenhagen, Denmark⁴⁹ Graduate School of Human and Environmental Studies, Kyoto University, Yoshida-Nihonmatsu, Sakyo, Kyoto 606-8501, Japan⁵⁰ Institute of Astronomy, Faculty of Physics, Astronomy, and Informatics, Nicolaus Copernicus University, Grudziadzka 5, 87-100 Torun, Poland⁵¹ Chungnam National University, Department of Astronomy and Space Science, 34134 Daejeon, Republic of Korea⁵² Department of Physics, Sharif University of Technology, P.O. Box 11365-9161, Tehran, Iran⁵³ Las Cumbres Observatory Global Telescope, 6740 Cortona Dr., Ste. 102, Goleta, CA 93111, USA⁵⁴ Department of Physics, University of California, Santa Barbara, CA 93106-9530, USA⁵⁵ Astrophysics Group, Keele University, Staffordshire, ST5 5BG, UK⁵⁶ Zentrum für Astronomie der Universität Heidelberg, Astronomisches Rechen-Institut, Mönchhofstraße 12-14, D-69120 Heidelberg, Germany⁵⁷ Center for Space Science, NYUAD Institute, New York University Abu Dhabi, P.O. Box 129188, Saadiyat Island, Abu Dhabi, UAE⁵⁸ Division of Science, New York University Abu Dhabi, P.O. Box 129188, Saadiyat Island, Abu Dhabi, UAE⁵⁹ Division of Engineering, New York University Abu Dhabi, P.O. Box 129188, Saadiyat Island, Abu Dhabi, UAE⁶⁰ Institut d'Astrophysique de Paris, Sorbonne Université, CNRS, UMR 7095, 98 bis bd Arago, F-75014 Paris, France⁶¹ SUPA, School of Physics & Astronomy, University of St. Andrews, North Haugh, St. Andrews KY16 9SS, UK⁶² National Astronomical Observatories, Chinese Academy of Sciences, 100012 Beijing, People's Republic of China⁶³ National Optical Astronomy Observatory, 950 N. Cherry Avenue, Tucson, AZ 85719, USA

Received 2021 April 2; revised 2021 April 26; accepted 2021 May 11; published 2021 July 29

Abstract

We report an analysis of the planetary microlensing event OGLE-2018-BLG-1185, which was observed by a large number of ground-based telescopes and by the *Spitzer* Space Telescope. The ground-based light curve indicates a low planet–host star mass ratio of $q = (6.9 \pm 0.2) \times 10^{-5}$, which is near the peak of the wide-orbit exoplanet mass-ratio distribution. We estimate the host star and planet masses with a Bayesian analysis using the measured angular Einstein radius under the assumption that stars of all masses have an equal probability of hosting the planet. The flux variation observed by *Spitzer* is marginal, but still places a constraint on the microlens parallax. Imposing a conservative constraint that this flux variation should be $\Delta f_{\text{Spz}} < 4$ instrumental flux units yields a host mass of $M_{\text{host}} = 0.37^{+0.35}_{-0.21} M_{\odot}$ and a planet mass of $m_{\text{p}} = 8.4^{+7.9}_{-4.7} M_{\oplus}$. A Bayesian analysis including the full parallax constraint from *Spitzer* suggests smaller host star and planet masses of $M_{\text{host}} = 0.091^{+0.064}_{-0.018} M_{\odot}$ and $m_{\text{p}} = 2.1^{+1.5}_{-0.4} M_{\oplus}$, respectively. Future high-resolution imaging observations with the *Hubble* Space Telescope or Extremely Large Telescope could distinguish between these two scenarios and help reveal the planetary system properties in more detail.

Unified Astronomy Thesaurus concepts: [Gravitational microlensing \(672\)](#); [Gravitational microlensing exoplanet detection \(2147\)](#); [Satellite microlensing parallax \(2148\)](#)

Supporting material: data behind figures

1. Introduction

The gravitational microlensing method has a unique sensitivity to low-mass planets (Bennett & Rhie 1996) beyond the snow line of the host star (Gould & Loeb 1992), where, according to core accretion theory predictions, planet formation is most efficient (Lissauer 1993; Pollack et al. 1996). The Microlensing Observations in Astrophysics (MOA) Collaboration (Bond et al. 2001; Sumi et al. 2003) presented the most complete statistical analysis of planets found by microlensing to date and the best measurement of the planet distribution beyond the snow line in Suzuki et al. (2016). They found that the mass-ratio distribution from the 2007 to 2012 MOA-II microlensing survey combined

with earlier samples (Gould et al. 2010; Cassan et al. 2012) is well fitted by a broken power-law model.

Their result shows the mass-ratio distribution peaks at $q_{\text{br}} = (6.7^{+9.0}_{-1.8}) \times 10^{-5}$ with power-law slopes of $n = -0.85^{+0.12}_{-0.13}$ and $p = 2.6^{+4.2}_{-2.1}$ above and below q_{br} , respectively.⁷⁰ This result is consistent with previous microlensing analyses, which suggest that Neptune-mass-ratio planets are more common than larger gas giants (Gould et al. 2006; Sumi et al. 2010), and further indicates that Neptune-mass-ratio planets are, in fact, the most common type of planet (large or small) in wide orbits.

Additionally, Suzuki et al. (2018) revealed a disagreement between the measured mass-ratio distribution in Suzuki et al. (2016) and the predictions of the runaway gas accretion scenario (Ida & Lin 2004), which is part of the standard core

⁶⁴ MOA Collaboration.⁶⁵ The *Spitzer* Team.⁶⁶ The KMTNet collaboration.⁶⁷ OGLE Collaboration.⁶⁸ MiNDSTeP Collaboration.⁶⁹ The ROME/REA Project Team.⁷⁰ These values are the median and 68% confidence level by Markov Chain Monte Carlo analysis with a 30-planet sample, which is given in Table 5 of Suzuki et al. (2016). So the 1σ range of the mass-ratio distribution peaks is roughly $q_{\text{br}} \sim (0.5\text{--}2) \times 10^{-4}$. At the same time, they also show that the best-fitting parameters are $q_{\text{br}} = 1.65 \times 10^{-4}$ with power-law slopes of $n = -0.92$ and $p = 0.47$ in Table 4 of Suzuki et al. (2016).

accretion theory. Population synthesis models based on core accretion, including runaway gas accretion, predict too few planets in the mass range of approximately $20\text{--}80M_{\oplus}$ compared to those inferred from microlensing observations. Similar tension is indicated by Atacama Large Millimeter/submillimeter Array (ALMA) observations. Nayakshin et al. (2019) compared the wide-orbit (9–99 au) planet candidates with masses of $0.01M_{\text{Jup}}$ to a few M_{Jup} suggested by ALMA protoplanetary disk observations to a population synthesis prediction from the runaway gas accretion scenario. They found that the scenario predicts fewer sub-Jovian planets than the ALMA observations inferred. Three-dimensional hydrodynamical simulations of protoplanetary disks do not support the runaway gas accretion scenario either (Lambrechts et al. 2019).

The peak position of the mass-ratio function and its slope at low-mass ratios are uncertain due to the lack of planets with mass ratios of $q < 5.8 \times 10^{-5}$ in the Suzuki et al. (2016) sample. Udalski et al. (2018) and Jung et al. (2019b) used samples of published planets to refine estimates of the peak and the low-mass-ratio slope of the mass-ratio function. Udalski et al. (2018) confirmed the turnover shown in Suzuki et al. (2016) and obtained the slope index in the low-mass regime, $p \sim 0.73$, using seven published planets with $q < 1 \times 10^{-4}$. Jung et al. (2019b) found $q_{\text{br}} \simeq 0.55 \times 10^{-4}$ using 15 published planets with low-mass ratios ($q < 3 \times 10^{-4}$). The Jung et al. (2019b) study was subject to “publication bias.” That is, the planets were not part of a well-defined statistical sample. Instead, these planets were selected for publication for reasons that are not well characterized. Nevertheless, the authors make the case that this publication bias should not be large enough to invalidate their results. By contrast, the Udalski et al. (2018) study only made the implicit assumption that all planets with $q < 1 \times 10^{-4}$ (and greater than that of the actual published planet) would have been published. If this is true (which is very likely), the study is not subject to publication bias.

A more definitive improvement of the Suzuki et al. (2016) mass-ratio function can be obtained with an extension of the MOA-II statistical sample to include additional microlensing seasons (D. Suzuki et al. 2021, in preparation). The low-mass-ratio planet analyzed in this paper, OGLE-2018-BLG-1185Lb, will be part of that extended sample, and it will contribute to an improved characterization of the low end of the wide-orbit exoplanet mass-ratio function.

The statistical analysis of the wide-orbit planet population can also be improved by including information on the lens physical parameters, such as the lens mass, M_L , and the distance to the lens star, D_L . While the lens planet–host mass ratios, q , are usually well constrained from the light-curve modeling, we need at least two mass–distance relations in order to derive M_L and D_L directly. There are three observables that can yield mass–distance relations: finite source effects, microlens parallax effects, and direct detection of the lens flux.

In recent years, lens flux detection by high-resolution imaging follow-up observations (such as by the Hubble Space Telescope (*HST*) or Keck) has been done for several microlens planetary systems after the lens and the source are separated enough to be detected (Bennett et al. 2006, 2007, 2015, 2020; Batista et al. 2014, 2015; Bhattacharya et al. 2017, 2018; Koshimoto et al. 2017; Vandenroux et al. 2020). However, the required separation for resolving the lens and source depends on their relative brightnesses, and even if they are comparable

in brightness, it typically takes a few years for them to separate sufficiently.

If both the Einstein radius θ_E from the finite source effect and the microlens parallax π_E from the parallax effect are measured, we can derive two mass–distance relations as follows:

$$M_L = \frac{c^2}{4G} \theta_E^2 \frac{D_S D_L}{D_S - D_L} = \frac{c^2}{4G} \frac{\text{au}}{\pi_E^2} \frac{D_S - D_L}{D_S D_L}, \quad (1)$$

where D_S is the distance to the source (Gould 1992, 2000). Finite source effects are detected in most planetary-lens events through the observation of a caustic crossing or a close approach to a caustic cusp, thus enabling the measurement of θ_E .

The most common method for measuring the microlens parallax has been via the effects of the motion of the observer, which is called the orbital parallax effect. In order to detect the orbital parallax, the ratio of t_E (typically t_E is ~ 30 days) to Earth’s orbital period (365 days) should be significant. Thus, we only measure the orbital parallax effect for microlensing events with long durations and/or relatively nearby lens systems, yielding mass measurements in less than half of the published microlensing planetary systems.

The most effective method for routinely obtaining a microlens parallax measurement is via the satellite parallax effect (Refsdal 1966), which is caused by the separation between two observers. Because the typical Einstein radius projected onto the observer plane, \tilde{r}_E , is about 10 au, the satellite parallax effect can be measured for a wide range of microlenses provided the separation between Earth and the satellite is about 1 au (as was the case for Spitzer).

For the purpose of measuring the Galactic distribution of planets and making mass measurements through the satellite parallax effect, the Spitzer microlensing campaign was carried out from 2014 to 2019 (Gould & Yee 2013; Gould et al. 2014, 2015a, 2015b, 2016, 2018). During the six-year program, close to 1000 microlensing events were simultaneously observed from the ground and by Spitzer, and there are 11 published⁷¹ planets with satellite parallax measurements from Spitzer: OGLE-2014-BLG-0124Lb (Udalski et al. 2015), OGLE-2015-BLG-0966Lb (Street et al. 2016), OGLE-2016-BLG-1067Lb (Calchi Novati et al. 2019), OGLE-2016-BLG-1195Lb (Shvartzvald et al. 2017), OGLE-2016-BLG-1190Lb (Ryu et al. 2018), OGLE-2017-BLG-1140Lb (Calchi Novati et al. 2018), TCP J05074264 + 2447555 (Nucita et al. 2018; Fukui et al. 2019; Zang et al. 2020), OGLE-2018-BLG-0596Lb (Jung et al. 2019), KMT-2018-BLG-0029Lb (Gould et al. 2020), OGLE-2017-BLG-0406Lb (Hirao et al. 2020), and OGLE-2018-BLG-0799Lb (Zang et al. 2020). Comparison of planet frequency in the disk to that in the bulge could probe the effects of the different environments on the planet formation process.

Obvious correlated noise in Spitzer photometry was first noted by Poleski et al. (2016) and Zhu et al. (2017), but those works did not expect the systematic errors would have a significant effect on the parallax measurements. Indeed, two comparisons of small, heterogeneous samples of published Spitzer microlensing events have confirmed this expectation (Shan et al. 2019; Zang et al. 2020). However, a larger study (Koshimoto & Bennett 2020) of the 50-event statistical sample of Zhu et al. (2017) indicated a conflict between the Spitzer

⁷¹ In addition Yee et al. (2021) have submitted a paper on OGLE-2019-BLG-0960.

microlensing parallax measurements and Galactic models. It suggested that this conflict was probably caused by systematic errors in Spitzer photometry. Based, in part, on the Koshimoto & Bennett (2020) analysis, the Spitzer microlensing team has made a greater effort to understand these systematic errors, including obtaining baseline data in 2019 for many of the earlier planetary events. These additional baseline data proved very useful in the characterization of systematics in Spitzer photometry for three previously published events (Gould et al. 2020; Hirao et al. 2020; Zang et al. 2020). Those analyses show that systematics in Spitzer photometry can be present at the level of 1–2 instrumental flux units, so observed signals in Spitzer photometry on those scales should be interpreted with caution.

In this paper, we present an analysis of the planetary microlensing event OGLE-2018-BLG-1185, which was simultaneously observed by many ground-based telescopes and the Spitzer Space Telescope. From ground-based light-curve analysis, the planet–host star mass ratio turns out to be very low, $q \sim 6.9 \times 10^{-5}$, which is thought to be near the peak of the wide-orbit exoplanet mass-ratio distribution in Suzuki et al. (2016), Udalski et al. (2018), and Jung et al. (2019b). Section 2 explains the observations and the data reductions. Our ground-based light-curve modeling method and results are shown in Section 3. In Section 4, we derive the angular Einstein radius from the source magnitude and color and the finite source effect in order to constrain the physical parameters of the planetary system. In Section 5, we estimate the physical properties such as the host star and planet masses based on the ground-based light curve alone by performing a Bayesian analysis using the measured angular Einstein radius under the assumption that stars of all masses have an equal probability of hosting the planet. We present our parallax analysis including the Spitzer data in Section 6. Finally, we discuss the analysis and summarize our conclusions in Section 7.

2. Observations and Data Reductions

2.1. Ground-based Survey Observations

The microlensing event OGLE-2018-BLG-1185 was first discovered on 2018 July 7 (HJD' = HJD – 2,450,000 \sim 8306), at J2000 equatorial coordinates (R.A., decl.) = (17^h59^m10^s.26, –27°50'06".3) corresponding to Galactic coordinates (l , b) = (2°465, –2°004), by the Optical Gravitational Lensing Experiment (OGLE) Collaboration (Udalski 2003). The OGLE Collaboration conducts a microlensing survey using the 1.3 m Warsaw Telescope with a 1.4 deg² field-of-view (FOV) CCD camera at Las Campanas Observatory in Chile and distributes alerts of the discovery of microlensing events by the OGLE-IV Early Warning System (Udalski et al. 1994; Udalski 2003). The event is located in the OGLE-IV field BLG504, which is observed with a cadence of one observation per hour.

The event was also discovered independently on 2018 July 9 by the MOA Collaboration and identified as MOA-2018-BLG-228 by the MOA alert system (Bond et al. 2001). The MOA Collaboration conducts a microlensing exoplanet survey toward the Galactic bulge using the 1.8 m MOA-II telescope with a 2.2 deg² wide FOV CCD camera, MOA-cam3 (Sako et al. 2008), at the University of Canterbury's Mount John Observatory in New Zealand. The MOA survey uses a custom wideband filter referred to as R_{MOA} , corresponding to the sum of the Cousins R and I bands, and also uses a Johnson V -band filter. The event is located

in the MOA field gb10, which is observed at a high cadence of one observation every 15 minutes. The Korea Microlensing Telescope Network (KMTNet) Collaboration (Kim et al. 2016) conducts a microlensing survey using three 1.6 m telescopes each with a 4.0 deg² FOV CCD camera. The telescopes are located at the Cerro Tololo Inter-American Observatory (CTIO) in Chile (KMTC), the South African Astronomical Observatory (SAAO) in South Africa (KMTS), and Siding Spring Observatory (SSO) in Australia (KMTA). This event is located in an overlapping region between two fields (KMTNet BLG03 and BLG43) and was identified by the KMTNet EventFinder (Kim et al. 2018) as KMT-2018-BLG-1024.

2.2. Spitzer Observations

In order to construct statistical samples from the Spitzer microlensing campaign, Yee et al. (2015) established detailed protocols for the selection and observational cadence of Spitzer microlensing targets. On 2018 July 8 (HJD' \sim 8308.25), OGLE-2018-BLG-1185 was selected as a “subjective, immediate” (SI) target to be observed with the “objective” cadence by the Spitzer microlensing team. The selection as SI meant that this event was observed even though it never met the objective criteria established in Yee et al. (2015). The Spitzer Space Telescope began to observe this event on 2018 July 14 (HJD' \sim 8313.83), which was 3 days after the peak observed from the ground-based telescopes. The objective cadence resulted in approximately one observation per day for the remainder of the observing window (27 days total). These observations were taken with the Infrared Array Camera in the 3.6 μm (L) band.

2.3. Ground-based Follow-up Observations

After the event was selected for Spitzer observations, some ground-based follow-up observations were conducted. The Microlensing Network for the Detection of Small Terrestrial Exoplanets (MiNDSTeP) used the 1.54 m Danish Telescope at La Silla Observatory in Chile and the 0.6 m telescope at Salerno University Observatory in Italy. The Microlensing Follow-up Network (μ FUN) used the 1.3 m SMARTS telescope at CTIO in Chile. Las Cumbres Observatory (LCO; Brown et al. 2013) used the 1.0 m telescopes at CTIO in Chile, at SSO in Australia, and at SAAO in South Africa, as part of an LCO–Spitzer program. The ROME/REA team (Tsapras et al. 2019) also used the 1.0 m LCO robotic telescopes at CTIO in Chile, at SSO in Australia, and at SAAO in South Africa. A summary of observations from each telescope is given in Table 1.

2.4. Data Reduction

The OGLE, MOA, and KMTNet data were reduced using the OGLE difference image analysis (DIA) photometry pipeline (Udalski 2003), the MOA DIA photometry pipeline (Bond et al. 2001), and the KMTNet pySIS photometry pipeline (Albrow et al. 2009), respectively. The MiNDSTeP data were reduced using DanDIA (Bramich 2008; Bramich et al. 2013). The μ FUN data were reduced using DoPHOT (Schechter et al. 1993), and the LCO data from the LCO–Spitzer program were reduced using a modified ISIS package (Alard & Lupton 1998; Alard 2000; Zang et al. 2018). The LCO data obtained by the ROME/REA team were reduced using a customized version of the DanDIA photometry pipeline. The Spitzer data were

Table 1
The Number of Data Points in the Light Curves and the Normalization Parameters

Name	Site	Collaboration	Aperture (m)	Filter	k	e_{\min}	$N_{\text{use}}/N_{\text{obs}}$
OGLE	Chile	OGLE	1.3	I	1.660	0.003	3045/3045
OGLE	Chile	OGLE	1.3	V	1.301	0.003	68/68
MOA	New Zealand	MOA	1.8	R_{MOA}	1.650	0.003	7277/7509
MOA	New Zealand	MOA	1.8	V	1.321	0.003	240/240
KMT SSO f03	Australia	KMTNet	1.6	I	1.900	0.003	2087/2706
KMT SSO f43	Australia	KMTNet	1.6	I	1.824	0.003	2080/2658
KMT CTIO f03	Chile	KMTNet	1.6	I	1.579	0.003	2304/2486
KMT CTIO f43	Chile	KMTNet	1.6	I	1.443	0.003	2195/2363
KMT SAAO f03	South Africa	KMTNet	1.6	I	2.444	0.003	1813/2096
KMT SAAO f43	South Africa	KMTNet	1.6	I	1.900	0.003	1846/2078
Danish	Chile	MinDSTeP	1.54	Z	1.015	0.003	139/154
Salerno	Italy	MinDSTeP	0.6	I	0/5
LCO SSO	Australia	LCO-Spitzer	1.0	i'	2.528	0.003	31/44
LCO CTIO	Chile	LCO-Spitzer	1.0	i'	1.129	0.003	17/17
LCO SAAO	South Africa	LCO-Spitzer	1.0	i'	0/19
CTIO 1.3 m	Chile	μFUN	1.3	I	0.852	0.003	18/18
CTIO 1.3 m	Chile	μFUN	1.3	V	0.566	0.003	3/3
LCO SSO	Australia	ROME/REA	1.0	g	0/25
LCO SSO	Australia	ROME/REA	1.0	i'	0/74
LCO SSO	Australia	ROME/REA	1.0	r	0/29
LCO CTIO	Chile	ROME/REA	1.0	g	1.110	0.003	33/33
LCO CTIO	Chile	ROME/REA	1.0	i'	1.589	0.003	61/61
LCO CTIO	Chile	ROME/REA	1.0	r	1.337	0.003	31/31
LCO SAAO	South Africa	ROME/REA	1.0	g	0/17
LCO SAAO	South Africa	ROME/REA	1.0	i'	0/19
LCO SAAO	South Africa	ROME/REA	1.0	r	0/45
Spitzer	Earth-trailing orbit	Spitzer	0.85	L	2.110	...	26/26

reduced using the photometry algorithm described in Calchi Novati et al. (2015).

It is known that the photometric error bars calculated by data pipelines can be underestimated (or more rarely overestimated). Various factors, such as observational conditions, can cause systematic errors. In order to get proper errors of the parameters in the light-curve modeling, we empirically normalize the error bars by using the standard method of Bennett et al. (2008). We use the formula

$$\sigma'_i = k\sqrt{\sigma_i^2 + e_{\min}^2}, \quad (2)$$

where σ'_i is the i th renormalized error, σ_i is the i th error obtained from DIA, and k and e_{\min} are the renormalizing parameters. We set the value of e_{\min} to account for systematic errors that dominate at high magnification, and we adjust the value of k to achieve $\chi^2/\text{dof} = 1$. The data from Salerno, LCO SAAO by the LCO-Spitzer program, and LCO SSO and SAAO by the ROME/REA project are too few to give any significant constraint or show systematics and disagreement with other data sets. Therefore, we do not use them for the modeling. We list the calculated error bar renormalization parameters in Table 1.

3. Ground-based Light-curve Analysis

3.1. Binary-lens model

The magnification of the binary-lens model depends on seven parameters: the time of lens-source closest approach, t_0 ; the Einstein radius crossing time t_E ; the impact parameter in units of the Einstein radius, u_0 ; the planet-host mass ratio q ; the

planet-host separation in units of the Einstein radius, s ; the angle between the trajectory of the source and the planet-host axis, α ; and the ratio of the angular source size to the angular Einstein radius, ρ . The model flux $f(t)$ of the magnified source at time t is given by

$$f(t) = A(t)f_s + f_b, \quad (3)$$

where $A(t)$ is the magnification of the source star, and f_s and f_b are the unmagnified flux from the source and the flux from any unresolved blend stars, respectively.

We also adopt a linear limb-darkening model for the source star,

$$S_\lambda(\vartheta) = S_\lambda(0)[1 - u_\lambda(1 - \cos(\vartheta))], \quad (4)$$

where $S_\lambda(\vartheta)$ is the limb-darkened surface brightness. The effective temperature of the source star estimated from the extinction-free source color presented in Section 4 is $T_{\text{eff}} \sim 5662$ K (González Hernández & Bonifacio 2009). Assuming a surface gravity $\log g = 4.5$ and a metallicity of $\log[\text{M}/\text{H}] = 0$, we select limb-darkening coefficients of $u_l = 0.5494$, $u_v = 0.7105$, $u_R = 0.6343$, $u_Z = 0.6314$, $u_g = 0.7573$, $u_r = 0.6283$, and $u_i = 0.5389$ from the ATLAS model (Claret & Bloemen 2011). For the R_{MOA} passband, we use the coefficient for $u_{\text{Red}} = 0.5919$, which is the mean of u_l and u_R .

We first conducted light-curve fitting with only ground-based data. We employed a Markov Chain Monte Carlo algorithm (Verde et al. 2003) combined with the image-centered ray-shooting method (Bennett & Rhie 1996; Bennett 2010). We conducted grid search analysis following the same procedure in Kondo et al. (2019). First, we performed a broad grid search over the (q, s, α) space with the other parameters

Table 2
The Best-fit Models for Ground-only Data

Parameters	Unit	2L1S (Close)	2L1S (Wide)	1L2S
χ^2/dof	...	23,221.473/23,252	23,489.306/23,252	23,601.431/23,249
$t_{0,1}$	HJD'	8310.7772 ± 0.0003	8310.7793 ± 0.0003	8310.7726 ± 0.0003
$t_{0,2}$	HJD'	8311.5874 ± 0.0010
t_E	days	15.931 ± 0.133	16.312 ± 0.144	15.730 ± 0.189
$u_{0,1}$	10^{-3}	6.877 ± 0.063	6.606 ± 0.067	7.777 ± 0.131
$u_{0,2}$	10^{-3}	8.773 ± 1.515
q	10^{-5}	6.869 ± 0.229	9.164 ± 0.552	...
s	...	0.963 ± 0.001	1.144 ± 0.003	...
α	rad	0.114 ± 0.001	3.261 ± 0.002	...
ρ_1	10^{-3}	3.468 ± 0.083	$<1.026^a$	7.234 ± 0.241
ρ_2	10^{-3}	1.613 ± 0.956
$q_{f,l}$	10^{-2}	1.699 ± 0.192
f_S (OGLE) ^b	...	107.777 ± 0.437	106.493 ± 0.448	108.583 ± 0.550
f_b (OGLE) ^b	...	396.165 ± 0.594	397.397 ± 0.440	393.516 ± 0.587

Notes.

^a The value is the 3σ upper limit.

^b All fluxes are on a 25th-magnitude scale, e.g., $I_S = 25 - 2.5 \log(f_S)$.

free. The search ranges of q , s , and α are $-6 < \log q < 0$, $-0.5 < \log s < 0.6$, and $0 < \alpha < 2\pi$, with 11, 22, and 40 grid points, respectively. Next, we refined all parameters for the best 100 models with the smallest χ^2 to search for the global best-fit model.

The parameters of the best-fit models are summarized in Table 2. The light curve and the caustic geometry are shown in Figures 1 and 2. As a result of the grid search, we found that the best-fit binary-lens model is favored over the single-lens model by $\Delta\chi^2 \sim 2330$. The bottom panels in Figure 1 show the clear deviations of the light curve with respect to the single-lens model from HJD' ~ 8310.9 to ~ 8311.8 , which are well fitted by the approach to the central caustic for the best binary-lens model. Although the additional magnification from the cusp approach to the planetary caustic is small, the asymmetric feature on the right side of the light curve due to the approach to the central caustic shows clear residuals from the single-lens model, which suggest the existence of a companion. The best binary-lens model suggests that the lens system has a very-low-mass ratio, $q \sim 6.9 \times 10^{-5}$, with a normalized separation $s \sim 0.96$. It is well known that there is a close/wide degeneracy in high-magnitude binary-lens events (Griest & Safizadeh 1998; Dominik 1999; Chung et al. 2005), which is due to the similar shape and size of the central caustic between s and s^{-1} . From the grid search, we found the best wide binary-lens model ($s > 1$) has $q \sim 9.2 \times 10^{-5}$ and $s \sim 1.14$. The separation of this wide model is slightly different from the reciprocal of the separation of the close model ($s < 1$), yielding a different shape and size for the central caustic from those of the best close model. We ruled out the wide model because the best close binary-lens model is favored over the wide model by $\Delta\chi^2 \sim 268$. The $\Delta\chi^2$ is large because the source trajectory is parallel to the lens axis and approaches not only the central caustic but also the planetary caustics.

3.2. Binary-source model

We checked the possibility that the observed light curve can be explained by the binary-source model because it is known that there is a possible degeneracy between the single-lens binary-source (1L2S) model and the binary-lens single-source (2L1S) model (Griest & Hu 1993; Gaudi 1998). For the 1L2S

model, the total effective magnification of the source stars A is expressed as follows:

$$A = \frac{A_1 f_1 + A_2 f_2}{f_1 + f_2} = \frac{A_1 + q_f A_2}{1 + q_f}, \quad (5)$$

where A_1 and A_2 are the magnification of the two sources with model flux f_1 and f_2 , respectively, and q_f is the flux ratio between the two sources ($= f_2/f_1$). In order to explain the magnification of the second source, we introduce additional parameters: the time of lens–source closest approach $t_{0,2}$, the impact parameter in units of the Einstein radius $u_{0,2}$, and the ratio of the angular source size to the angular Einstein radius, ρ_2 . We found the best-fit 1L2S model is disfavored relative to the best-fit 2L1S model by $\Delta\chi^2 \sim 380$, and we excluded the 1L2S model. The parameters of the best-fit 1L2S model are summarized in Table 2. The light curve of the 1L2S model is shown in Figure 1.

3.3. Ground-based Parallax

The magnification of the binary-lens model with parallax effects needs two additional parameters: the north and east components of the parallax vector π_E in equatorial coordinates, $\pi_{E,N}$ and $\pi_{E,E}$ (Gould 2004). The orbital parallax effects are caused by Earth's orbital motion. In the case of OGLE-2018-BLG-1185, the timescale, $t_E \sim 15.9$ days, is small compared to Earth's orbital period, which makes it less likely for us to measure the parallax effects. The best-fit parallax model improves the fit slightly by $\Delta\chi^2 \sim 20$, but there is disagreement in χ^2 improvement between the data sets. The parallax information such as the direction and the value is easily influenced by the systematics in each telescope data set. Considering these facts, we concluded that we should disregard the parallax information from the ground-based data.

4. Angular Einstein Radius

We can estimate the angular Einstein radius $\theta_E = \theta_*/\rho$ because ρ can be derived by the light-curve fitting and the angular source radius θ_* can be derived by using an empirical

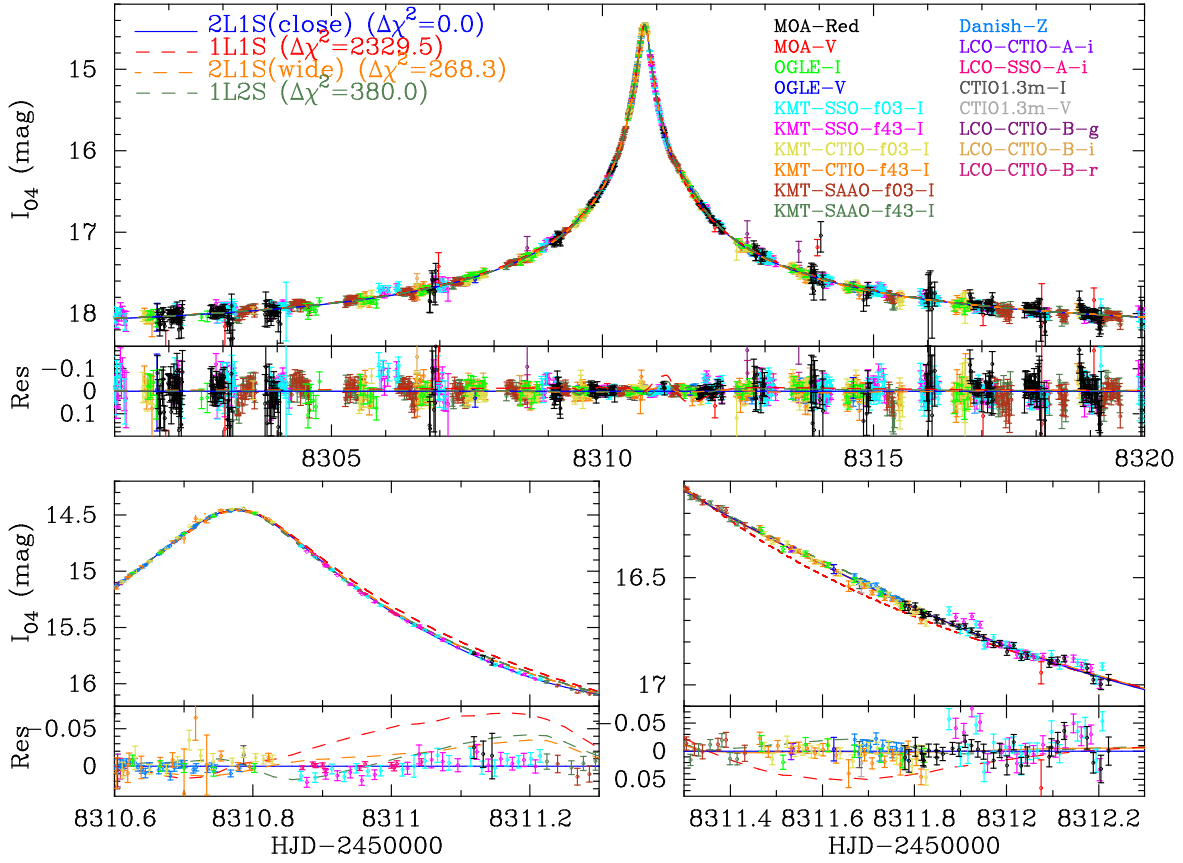


Figure 1. The light curve and models with the ground-based data for OGLE-2018-BLG-1185. The top panel shows the light curve, models, and residuals from the best-fit close binary-lens (2L1S) model. The blue line shows the best-fit close 2L1S model. The red, orange, and green dotted lines show the single-lens (1L1S) model, the wide 2L1S model, and the binary-source (1L2S) model, respectively. The left and right bottom panels show zoomed-in views of the light curve, where we can find clear deviations of the data points from the 1L1S and 1L2S models.

(The data used to create this figure are available.)

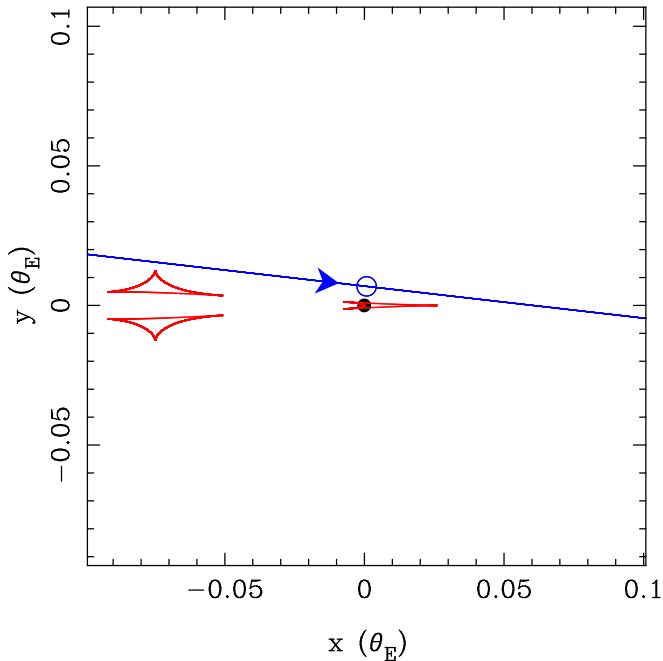


Figure 2. Caustic geometry of the best-fit model. The caustics are shown as red lines. The blue line shows the source trajectory on the lens plane and the arrow indicates the direction of the source/lens relative proper motion. The blue open circle indicates the source size and position at t_0 .

relation between θ_* , the extinction-corrected source color ($V - I_{S,0}$), and the magnitude $I_{S,0}$ (e.g., Boyajian et al. 2014).

We derived the OGLE-IV instrumental source color and magnitude from the light-curve fitting and then converted them to the standard ones by using the following color-color relation from Udalski et al. (2015):

$$I_{03} - I_{04} = (0.182 \pm 0.015) + (-0.008 \pm 0.003)(V - I)_{03}, \quad (6)$$

$$V_{03} - V_{04} = (0.257 \pm 0.015) + (-0.074 \pm 0.004)(V - I)_{03}. \quad (7)$$

The apparent color and the standard magnitude of the source star are $(V - I, I_{S,0,calib}) = (2.344 \pm 0.031, 20.082 \pm 0.012)$.

We also derived the apparent source color and magnitude from the CT13 measurements in the I and V bands from the light-curve fitting, and then converted them to the standard ones following the procedure explained in Bond et al. (2017). We cross-referenced isolated stars in the CT13 catalog reduced by DoPHOT (Schechter et al. 1993) with the stars in the OGLE-III map within $120''$ of the source star and obtained the color-color relations

$$I_{03} - I_{CT13} = (-0.880 \pm 0.005) + (-0.042 \pm 0.005)(V - I)_{CT13}, \quad (8)$$

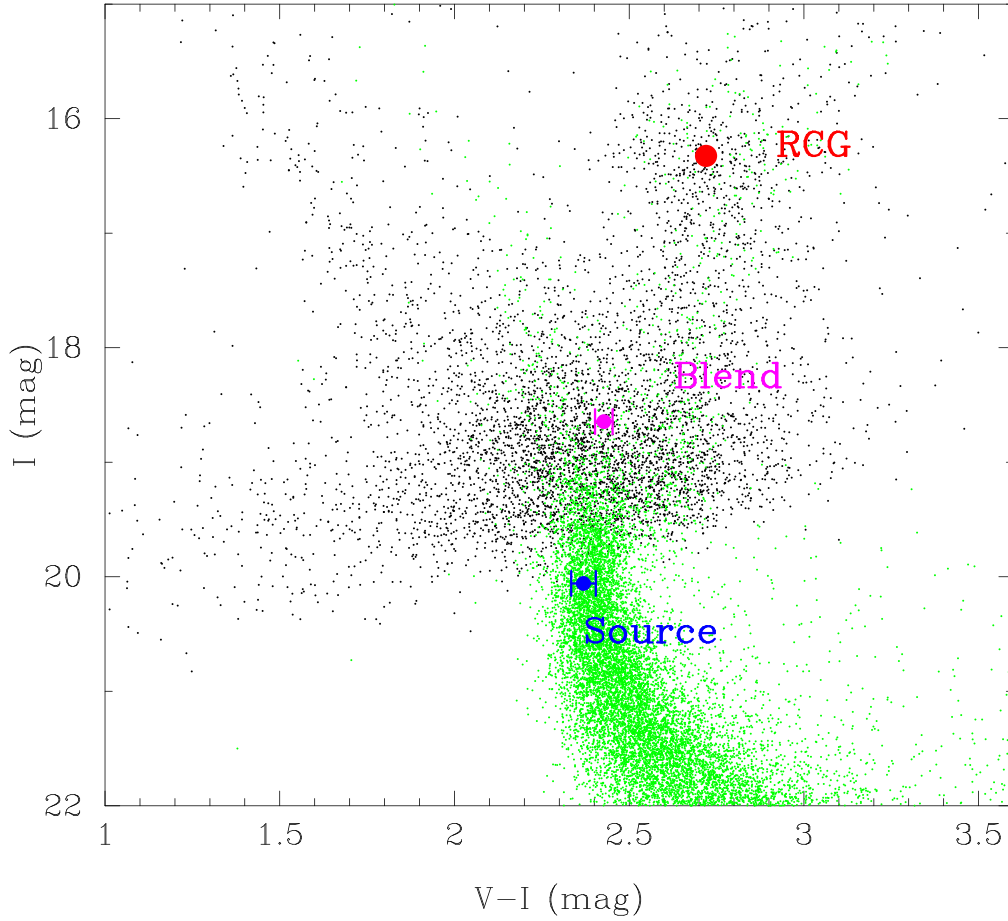


Figure 3. The CMD. The stars in the OGLE-III catalog within $120''$ of the source star are shown as black dots. The green dots indicate the *HST* CMD of Holtzman et al. (1998), which is transformed to the same reddening and extinction of the field of the event. The red dot shows the centroid of the RCG distribution. The colors and magnitudes of the source star and the blend are shown in blue and pink, respectively.

$$V_{03} - I_{CT13} = (1.290 \pm 0.004) + (-0.036 \pm 0.004)(V - I)_{CT13}. \quad (9)$$

The apparent color and magnitude of the source star are $(V - I, I)_{S,CT13,calib} = (2.335 \pm 0.025, 20.105 \pm 0.013)$. This color is consistent with $(V - I)_{S,O4,calib}$ within 1σ and the magnitude is consistent with $I_{S,O4,calib}$ within 2σ . Because the light curve was well covered by the OGLE observations, while it was highly magnified, we adopted $(V - I, I)_{S,O4,calib}$ as the source color and magnitude.

To obtain the extinction-corrected source color and magnitude, we used the standard method from Yoo et al. (2004). The intrinsic color and magnitude are determined from the source location relative to the color and magnitude of the red clump giant (RCG) centroid in the color-magnitude diagram (CMD). In Figure 3, the red point shows the RCG centroid color and magnitude, $(V - I, I)_{RCG} = (2.720, 16.325) \pm (0.009, 0.032)$, for the field around the source star. Assuming that the source star suffers the same reddening and extinction as the RCGs, we compared these values to the expected extinction-corrected RCG color and magnitude for this field, $(V - I, I)_{RCG,0} = (1.060, 14.362) \pm (0.070, 0.040)$ (Bensby et al. 2013; Nataf et al. 2013). As a result, we obtained an extinction of $A_I = 1.963 \pm 0.051$ and a color excess of $E(V - I) = 1.660 \pm 0.071$. Finally, the intrinsic source color and magnitude were derived:

$$(V - I, I)_{S,0} = (0.684, 18.119) \pm (0.077, 0.053). \quad (10)$$

As a reference for later discussion of future follow-up observations, we also estimated the intrinsic source magnitudes in the *H* and *K* bands from the color-color relation in Kenyon & Hartmann (1995), including a 5% uncertainty. Then, we applied the extinction in the *H* and *K* bands, which was derived from the extinction in the *I* and *V* bands of the RCGs according to Cardelli et al. (1989).

Figure 3 shows that the source is consistent with being part of the standard bulge sequence of stars, i.e., it falls within the distribution of stars from Holtzman et al. (1998) after they have been shifted to the same reddening and extinction as the field for OGLE-2018-BLG-1185. However, the source also has a similar color to the Sun. Thus, it would also be consistent with having an absolute magnitude similar to that of the Sun but being somewhat in the foreground, e.g., at ~ 6 kpc. Thus, we also checked how a different assumption about the source would affect our results. If the source was more in the foreground, it would then suffer less extinction and reddening than the RCGs. However, even if we assume 10% less extinction and reddening than those of the RCGs, the value of θ_E increases by only 7%, which is still consistent within 1σ with values obtained assuming the same extinction and reddening as those of the RCGs. We summarize the source colors and magnitudes in Table 3.

Applying the empirical formula $\log(\theta_{LD}) = 0.501414 + 0.419685(V - I) - 0.2I$ (see Fukui et al. 2015 but also

Table 3
The Source Colors and Magnitudes

Parameters	Unit	Source (Apparent)	Source (Intrinsic) ^a	Source (Intrinsic) ^b
I	mag	20.082 ± 0.012^c	18.119 ± 0.053	18.315 ± 0.053
$V - I$	mag	2.344 ± 0.031^c	0.684 ± 0.077	0.850 ± 0.077
H^d	mag	18.012 ± 0.143	17.444 ± 0.095	...
K^d	mag	17.756 ± 0.145	17.394 ± 0.095	...

Notes.

^a Extinction-corrected magnitudes assuming that the source star suffers the same reddening and extinction as the RCGs.

^b Extinction-corrected magnitudes assuming that the source star suffers reddening and extinction 0.9 times those of the RCGs.

^c The magnitude and color are measured from the light-curve fitting.

^d The magnitudes are estimated from the color–color relation in Kenyon & Hartmann (1995) and the extinction law in Cardelli et al. (1989).

Boyajian et al. 2014), where $\theta_{LD} \equiv 2\theta_*$ is the limb-darkened stellar angular diameter, we found the angular source radius,

$$\theta_{LD} = 1.461 \pm 0.109 \mu\text{as}, \quad (11)$$

$$\theta_* = 0.730 \pm 0.059 \mu\text{as}. \quad (12)$$

Finally, we obtained the source angular radius and the lens–source relative proper motion in the geocentric frame:

$$\theta_E = \frac{\theta_*}{\rho} = 0.211 \pm 0.018 \text{ mas}, \quad (13)$$

$$\mu_{\text{rel,geo}} = \frac{\theta_E}{t_E} = 4.832 \pm 0.410 \text{ mas yr}^{-1}. \quad (14)$$

This θ_E value is relatively small, which suggests that the lens is a low-mass star and/or distant from the observer.

5. Lens Physical Parameters by Bayesian Analysis

If we can measure both the finite source effects and the parallax effects, the lens physical parameters such as the host mass M_{host} and the distance to the lens D_L are calculated directly, following the equations

$$M_{\text{host}} = \frac{\theta_E}{(1+q)\kappa\pi_E}; \quad D_L = \frac{\text{au}}{\pi_{\text{rel}} + \pi_S};$$

$$\pi_{\text{rel}} = \theta_E \pi_E; \quad \mu_{\text{rel}} = \frac{\theta_E \pi_E}{t_E}, \quad (15)$$

where $\kappa \equiv 4G/(c^2 \text{au}) = 8.1439 \text{ mas}/M_\odot$, and $\pi_S = \text{au}/D_S$ is the source parallax. From the ground-based light curve alone, we are only able to measure θ_E (via finite source effects), and find no meaningful constraint on π_E (see Section 3.3).

In order to estimate the probability distributions of M_L and D_L , we conducted a Bayesian analysis with the Galactic model of Koshimoto et al. (2021a).⁷² We randomly generated a 50 million simulated microlensing event sample. Then we calculated the probability distributions for the lens physical parameters by weighting the microlensing event rate by the measured t_E and θ_E likelihood distribution. It is important to note that we conducted the Bayesian analysis under the

assumption that stars of all masses have an equal probability of hosting the planet.

We calculated some parameters in addition to the lens physical parameters, M_L and D_L . For instance, the lens–source proper motion in the geocentric frame, μ_{rel} , is converted to that in the heliocentric frame,

$$\mu_{\text{rel,hel}} = \mu_{\text{rel}} + v_{\oplus,\perp} \frac{\pi_{\text{rel}}}{\text{au}}, \quad (16)$$

where $v_{\oplus,\perp} = (v_{\oplus,N}, v_{\oplus,E}) = (-0.78, 27.66) \text{ km s}^{-1}$ is the projected velocity of Earth at t_0 .

We also calculated the I - and V -band magnitudes of the lens from the mass–luminosity relations of main-sequence stars (Kenyon & Hartmann 1995), and the 5 Gyr isochrone for brown dwarfs from Baraffe et al. (2003). Then we estimated the H - and K -band magnitudes of the lens from the color–color relation in Kenyon & Hartmann (1995), including a 5% uncertainty. In order to estimate the extinction in the foreground of the lens, we assumed a dust scale height of $h_{\text{dust}} = 0.10 \pm 0.02 \text{ kpc}$ (Bennett et al. 2015):

$$A_{\lambda,L} = \frac{1 - e^{-|D_L/(h_{\text{dust}} \sin b)|}}{1 - e^{-|D_S/(h_{\text{dust}} \sin b)|}} A_{\lambda,S}, \quad (17)$$

where the index λ refers to the passband: the V , I , H , or K band. We obtained the extinction in the I - and V -band magnitudes of the source from the RCGs in Section 4, and then we converted it to the extinction in the H and K bands according to Cardelli et al. (1989).

The results are shown in Table 4 and Figure 4. According to Figure 4, the lens system is likely to be a super-Earth with a mass of $m_p = 8.1^{+7.6}_{-4.4} M_\oplus$ orbiting a late M dwarf with a mass of $M_{\text{host}} = 0.36^{+0.33}_{-0.19} M_\odot$ at a projected separation of $a_\perp = 1.54^{+0.18}_{-0.22} \text{ au}$. The system is located at $D_L = 7.4^{+0.5}_{-0.9} \text{ kpc}$ from Earth. For reference, we also plot the source magnitudes in the V , I , H , and K bands as red lines; the H - and K -band magnitudes were estimated in Section 4. We also show the parallax contour derived from the Bayesian analysis in Figure 5.

6. Analysis Including Spitzer Data

We measure the microlens parallax vector π_E via the satellite parallax effect, which can be approximated as

$$\pi_E = \frac{\text{au}}{D_\perp} \left(\frac{t_{0,\text{sat}} - t_{0,\oplus}}{t_E}, u_{0,\text{sat}} - u_{0,\oplus} \right), \quad (18)$$

where D_\perp is the Earth–satellite separation projected on the plane of the sky, and $t_{0,\text{sat}}$ and $u_{0,\text{sat}}$ are the time of lens–source closest approach and the impact parameter as seen by the satellite. The Einstein timescale t_E is assumed to be the same for both Earth and the satellite. In practice, we fully model Spitzer’s location as a function of time.

The Spitzer light curve for OGLE-2018-BLG-1185 shows a very weak decline of $\Delta f_{\text{Spz}} \sim 1$ flux unit over the four-week observation period (see Figure 6). This change (rather than, e.g., the value of the flux at the start of observations) is the most robust constraint because it is independent of the unknown blended light. However, the magnitude of the decline is comparable to the level of systematics seen in a few other events (Gould et al. 2020; Hirao et al. 2020; Zang et al. 2020) and thus should be treated with caution. At the same time, even

⁷² The code for microlensing simulation using the Galactic model has been published (Koshimoto & Ranc 2021b) and can be downloaded at <https://github.com/nkoshimoto/genulens> as a prior.

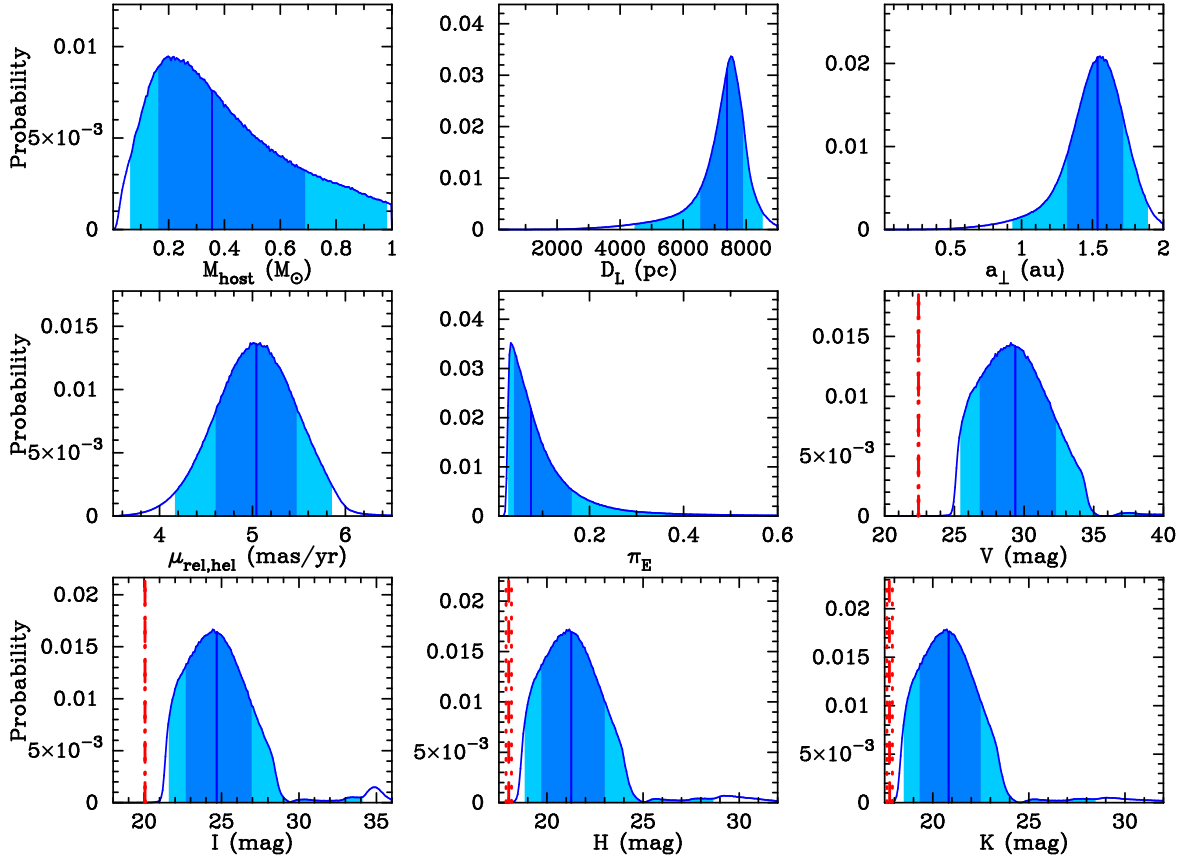


Figure 4. Probability distribution of lens properties derived from the Bayesian analysis with a Galactic prior and constrained by t_E and θ_E . The vertical blue lines show the median values. The dark-blue and light-blue regions show the 68.3% and 95.4% confidence intervals. The vertical red lines in the probability distributions of the I -, V -, H -, and K -band magnitudes show the magnitudes of the source star with extinction.

Table 4
The Lens Physical Parameters

Parameters	Unit	Bayesian			Naive Spitzer-only	
		Ground-only	Ground + Δf_{Spz}	Ground + π_E, Spz	($u_0 > 0$)	($u_0 < 0$)
M_{host}	M_{\odot}	$0.36^{+0.33}_{-0.19}$	$0.37^{+0.35}_{-0.21}$	$0.091^{+0.064}_{-0.018}$	0.073 ± 0.011	0.070 ± 0.010
m_p	M_{\oplus}	$8.1^{+7.6}_{-4.4}$	$8.4^{+7.9}_{-4.7}$	$2.1^{+1.5}_{-0.4}$	1.7 ± 0.3	1.6 ± 0.2
D_L	kpc	$7.40^{+0.51}_{-0.85}$	$7.40^{+0.51}_{-0.88}$	$5.45^{+1.70}_{-0.66}$	4.96 ± 0.74	4.89 ± 0.66
a_{\perp}	au	$1.54^{+0.18}_{-0.22}$	$1.54^{+0.18}_{-0.22}$	$1.14^{+0.32}_{-0.15}$	1.01 ± 0.18	0.99 ± 0.16
π_E	...	$0.075^{+0.087}_{-0.036}$	$0.073^{+0.093}_{-0.035}$	$0.292^{+0.066}_{-0.120}$	0.354 ± 0.042	0.369 ± 0.037
$\mu_{\text{rel, hel}}$	mas yr^{-1}	$5.04^{+0.43}_{-0.44}$	$5.06^{+0.43}_{-0.44}$	4.86 ± 0.44
V	mag	$29.4^{+2.9}_{-2.6}$	$29.3^{+3.1}_{-2.6}$	$34.1^{+5.2}_{-1.6}$
I	mag	$24.7^{+2.3}_{-2.0}$	$24.6^{+2.4}_{-2.0}$	$28.2^{+3.4}_{-1.2}$
H	mag	$21.3^{+1.7}_{-1.6}$	$21.2^{+1.9}_{-1.6}$	$23.9^{+2.6}_{-0.9}$
K	mag	$20.8^{+1.7}_{-1.5}$	$20.8^{+1.8}_{-1.5}$	$23.3^{+2.9}_{-0.8}$

this weak decline indicates a significant parallax effect for the event as seen from Spitzer. We derive a color constraint for the Spitzer data by measuring the IHL color-color relation for clump stars in CT13 I and H , and Spitzer L . Evaluating this relation at the measured $(I - H)$ color of the source gives a constraint on the Spitzer source flux:

$$I_{\text{CT13}} - L = -4.518 \pm 0.028, \quad (19)$$

which gives an expected source flux from Spitzer of $f_{\text{S,Spz}} = 0.6254$ flux units for the best-fit value of I_{CT13} . This constraint and the best-fit ground-based model (Table 4) together

imply some tension with the observed Spitzer light curve unless there is a significant parallax effect. They predict that the observed Spitzer flux should have been substantially brighter at the start of the Spitzer observations ($f_{\text{Spz}}(\text{HJD}') = 8313.83) \sim 6$ flux units) and declined by a total of $\Delta f_{\text{Spz}} \sim 3.3$ flux units as compared to the observed $\Delta f_{\text{Spz}} \sim 1$ flux unit. This tension can be seen in Figure 6 and suggests that, due to the parallax effect, the event peaked at a lower magnification and/or earlier as seen from Spitzer.

We can use limits on the change in Spitzer flux (Δf_{Spz}) to place conservative constraints on the physical properties of the

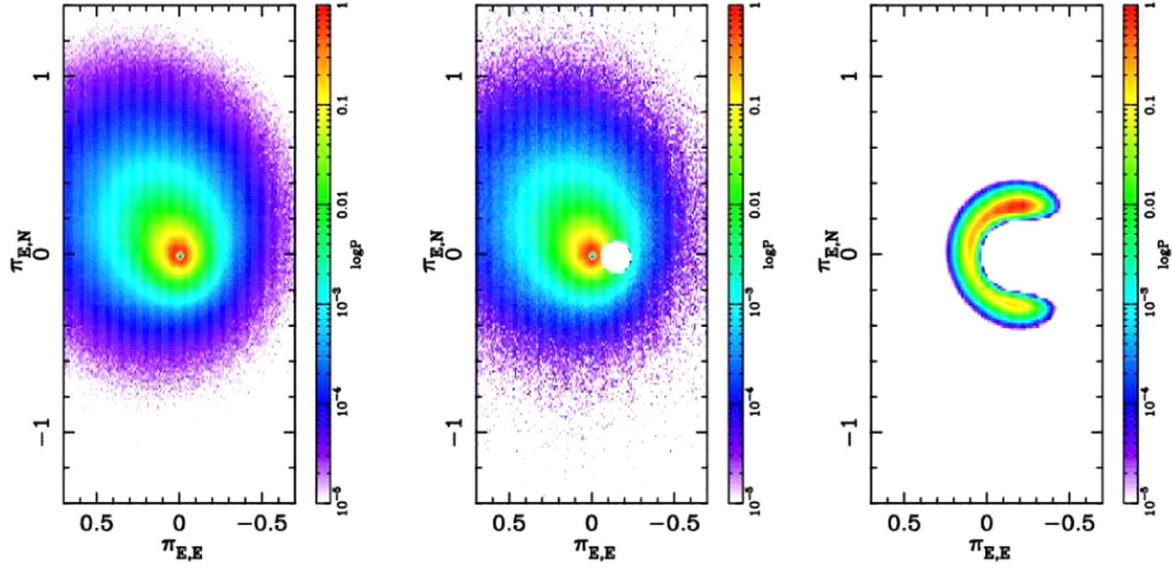


Figure 5. Left: The parallax contours for OGLE-2018-BLG-1185 expected from the Galactic model of Koshimoto et al. (2021a) after imposing the two observational constraints of the angular Einstein radius, θ_E , and the Einstein radius crossing time, t_E , on the event rate. The colorbar corresponds to the logarithm of the event rate and the red region indicates higher probability. Center: Including the constraint that $\Delta f_{\text{Spz}} < 4$. Right: Including the full constraint from the Spitzer-only parallax.

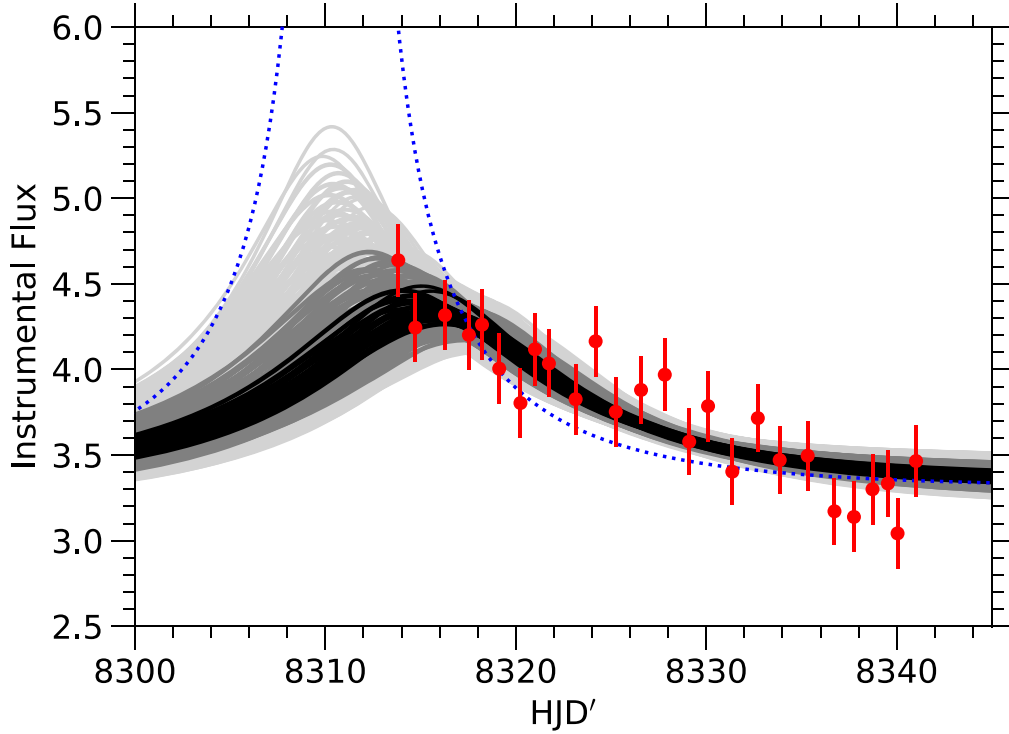


Figure 6. The light curve and models with the Spitzer data. The blue dotted line shows the Spitzer flux predicted by the 2L1S best-fit model derived from the ground-based analysis for $\pi_E = (0, 0)$ evaluated at the central value of the color constraint. The black and gray shaded regions show the models derived from the Spitzer-only parallax analysis. Each color (black, dark gray, and light gray) represents $\Delta\chi^2 < (1, 4, 9)$.

(The data used to create this figure are available.)

lens. Suppose that systematics affect the Spitzer light curve at the level of 1–2 flux units, i.e., at the level seen in previous work. If the true signal is $\Delta f_{\text{Spz}} \sim 4$ flux units, it is very unlikely that systematics would cause us to measure $\Delta f_{\text{Spz}} = 1$ flux unit. Therefore, we repeat the Bayesian analysis imposing the constraint $\Delta f_{\text{Spz}} < 4$, where Δf_{Spz} is calculated from Equation (19). The parallax effect can produce a degeneracy

in the sign of u_0 . In this case, because u_0 is small, the effect of this degeneracy is much smaller than the uncertainties (Gould & Yee 2012), so we only carry out this calculation for the $u_0 > 0$ case.

The results are given in Table 4 (as “Ground + Δf_{Spz} ”), Figure 7, and the center panel of Figure 5. This constraint suggests an $M_{\text{host}} = 0.37^{+0.35}_{-0.21} M_{\odot}$ host with an $m_p = 8.4^{+7.9}_{-4.7} M_{\oplus}$ planet at

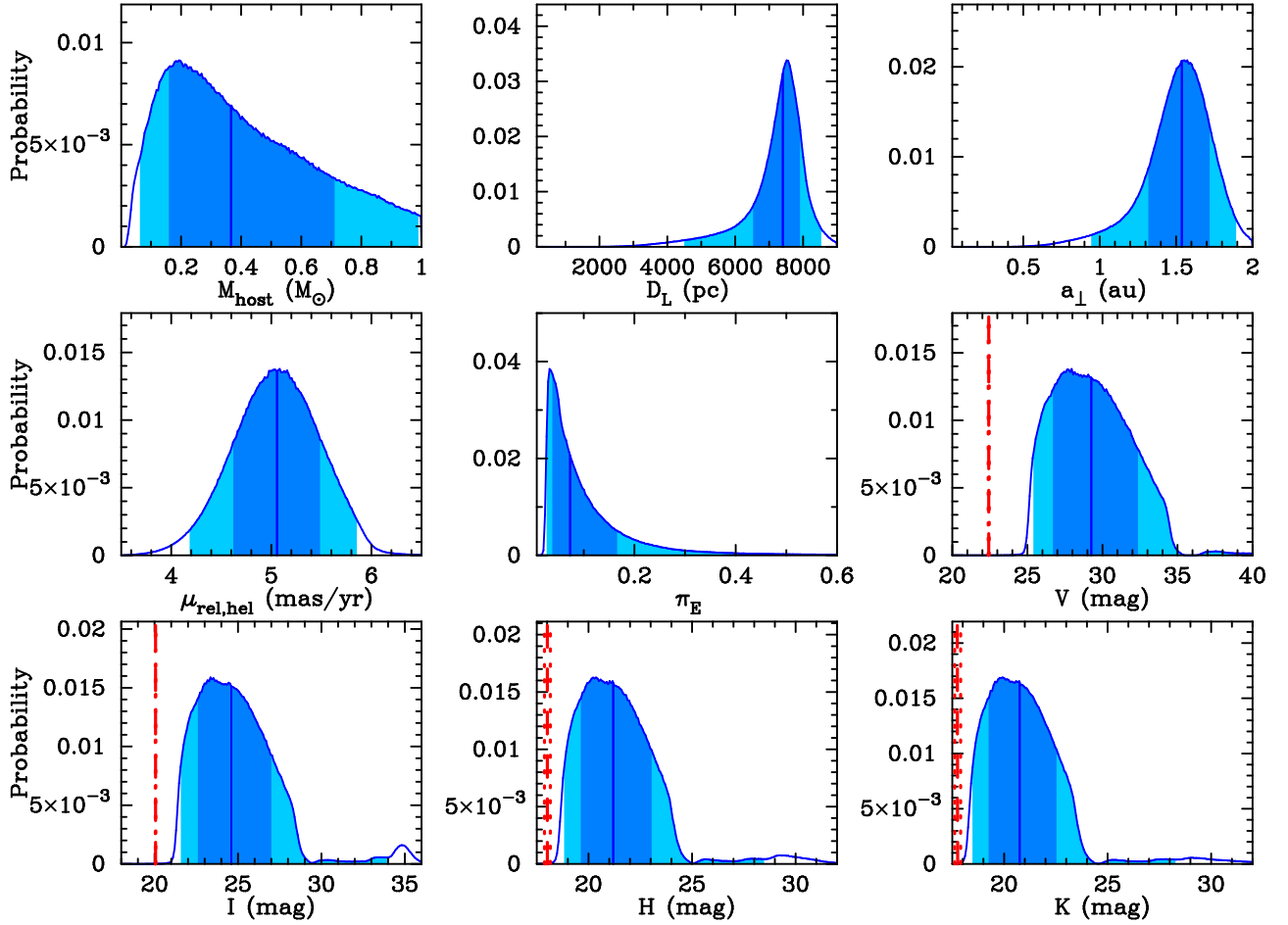


Figure 7. Same as Figure 4, but with the addition of the constraint $\Delta f_{\text{Spz}} < 4$.

a projected separation $a_{\perp} = 1.54^{+0.18}_{-0.22}$ au. We adopt these values as our conservative Bayesian estimates of the properties of the lens system.

6.1. Spitzer-only Parallax

If we take the Spitzer light curve at face value, we can derive stronger constraints on the parallax using the Spitzer-only parallax method. This method has been used in several previous analyses (starting with Gould et al. 2020) to show how the Spitzer light curve constrains the parallax. For this analysis, we hold the microlensing parameters t_0 , u_0 , and t_E fixed at values found by fitting the ground-based data and make the assumption that the Spitzer light curve is in the point lens regime.⁷³ Then, for a grid of parallax values, we fit for the Spitzer flux while applying the color constraint from Equation (19). We repeat the analysis for $-u_0$, which produces an indistinguishable ground-based light curve and, as expected, only slight variations in the parallax.

The resulting parallax contours are shown in Figure 8. The four minima correspond to the well-known satellite parallax degeneracy (Refsdal 1966; Gould 1994) and the overall arc shape follows the expectation from the Gould (2019) osculating circle formalism. The values for the magnitude of the microlens parallax vector are $\pi_E = 0.35 \pm 0.04$ for the ($u_0 > 0$) case and

$\pi_E = 0.37 \pm 0.04$ for the ($u_0 < 0$) case. The 3σ ranges are $\pi_E = [0.18, 0.50]$ and $\pi_E = [0.20, 0.48]$, respectively.

6.2. Physical Lens Properties from Spitzer Parallax

We can derive the physical properties of the lens by combining the measurement of the parallax from the Spitzer-only analysis with the measurement of $\theta_E = 0.211 \pm 0.019$ mas from fitting the ground-based light curve. These estimates and their uncertainties are derived from Equation (15) using simple error propagation, and so are the naive values of these quantities. For the ($u_0 > 0$) solution, this yields a lens mass of $M_L = 0.073 \pm 0.011 M_{\odot}$ and $D_L = 4.96 \pm 0.74$ kpc for $D_S = 7.88$ kpc. This would then imply that the mass of the planet is $m_p = 1.7 \pm 0.3 M_{\oplus}$ and that it is separated from the host by $a_{\perp} = 1.01 \pm 0.18$ au. The values for the ($u_0 < 0$) solution are comparable. See Table 4.

In order to estimate the lens magnitude, we also performed a Bayesian analysis including the π_E constraint derived from the Spitzer-only parallax analysis. First, we took the average of the χ^2 values for the two ($u_0 > 0$) and ($u_0 < 0$) solutions for each value of $\pi_{E,E}$ and $\pi_{E,N}$. Then, the event rate was weighted by $\exp(-\Delta\chi^2/2)$ and the measured t_E and θ_E constraints to calculate the probability distribution. Table 4 and Figure 9 show the results. The distributions for some of the parameters in Figure 9 are bimodal. In addition to the expected peak for lenses at $D_L \sim 5$ kpc, there is a second peak for lenses with $D_L \sim 7.5$ kpc. This second peak corresponds to events with

⁷³ In principle, we should calculate the Spitzer magnification using the full planetary model, but in practice, this makes almost no difference because the Spitzer observations start well after the planetary perturbation.

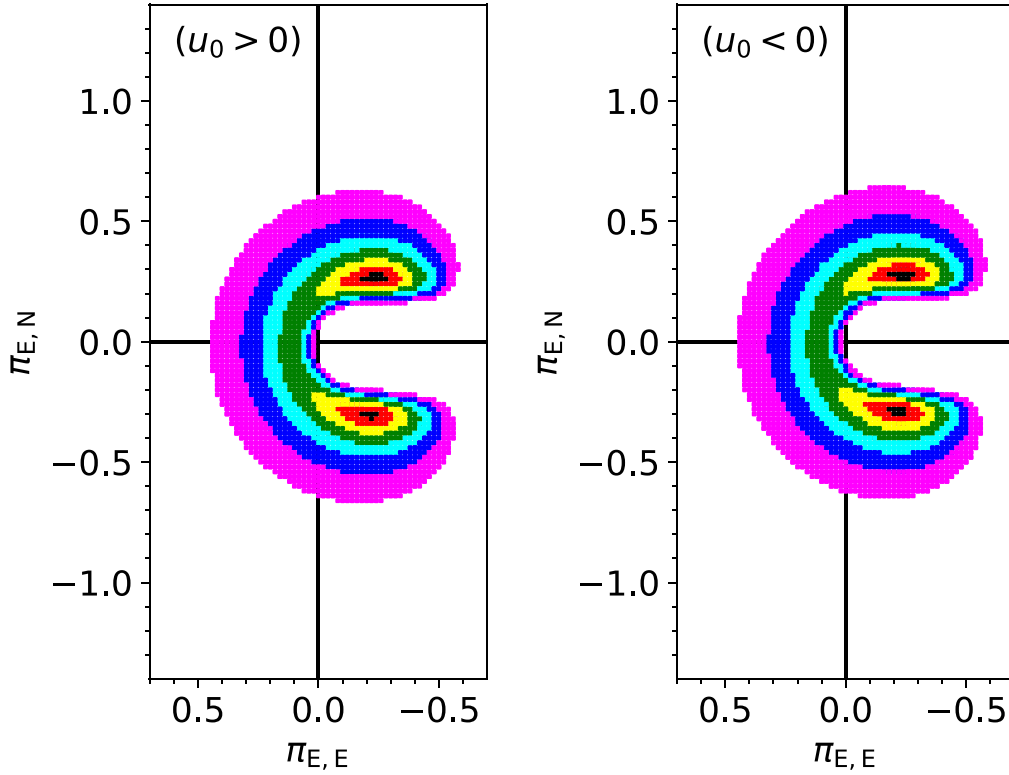


Figure 8. Parallax contours from Spitzer-only analysis (see text). The colors—black, red, yellow, green, cyan, blue, and magenta—indicate 1σ , 2σ , 3σ , 4σ , 5σ , 6σ , and 7σ from the minimum, respectively. The left panel is for $(u_0 > 0)$ and the right panel is for $(u_0 < 0)$.

lenses in the bulge and sources in the far disk, which were not considered in our naive calculations. For the bimodal distributions, the central values and confidence intervals reported in Table 4 are not a complete description of the distributions and should be considered in the context of Figure 9. However, the mass distribution is not subject to this issue. We find that the lens system is likely to be a terrestrial planet with a mass of $m_p = 2.1^{+1.5}_{-0.4} M_\oplus$ orbiting a very low mass (VLM) dwarf with a mass of $M_{\text{host}} = 0.091^{+0.064}_{-0.018} M_\odot$.

6.3. Implications

Hence, if the Spitzer-only parallax is correct, this would be the second detection of a terrestrial planet orbiting a VLM dwarf from the Spitzer microlensing program. The first was OGLE-2016-BLG-1195Lb (Bond et al. 2017; Shvartzvald et al. 2017), which is an $m_p = 1.43^{+0.45}_{-0.32} M_\oplus$ planet orbiting an $M_L = 0.078^{+0.016}_{-0.012} M_\odot$ VLM dwarf at a separation of $a_L = 1.16^{+0.16}_{-0.13}$ au. The distance to the OGLE-2016-BLG-1195L system is also comparable: $D_L = 3.91^{+0.42}_{-0.46}$ kpc. One curiosity about OGLE-2016-BLG-1195L is that the lens-source relative proper motion suggests that the lens could be moving counter to the direction of Galactic rotation, which would be unusual for a disk lens.

Therefore, we also consider the implications of the Spitzer-only π_E for constraining the lens motion in OGLE-2018-BLG-1185. First, we note that there is no independent information on the proper motion of the source μ_S because there is no evidence that the blend, which dominates the baseline object, is associated with the event (see Appendix). Second, given $D_L \sim 4.9$ kpc, we assume that the lens is in the disk and

therefore has a proper motion similar to that of other disk stars. The velocity model of Koshimoto et al. (2021a) is based on the Shu distribution function model in Sharma et al. (2014), but the mean velocity and velocity dispersion in the disk are fitted to the Gaia DR2 data (Gaia Collaboration et al. 2018) as a function of the Galactocentric distance, R , and the height from the Galactic plane, z . The velocity of disk stars at 4.9 kpc is $(v_\phi, v_z) = (207.6^{+42.7}_{-44.0}, -0.4^{+38.8}_{-39.6}) \text{ km s}^{-1}$. Hence, for the velocity dispersion, we use $(\sigma_{v,\phi}, \sigma_{v,z}) = (43.4, 39.2) \text{ km s}^{-1}$. Table 5 summarizes the disk star velocities and proper motions expected from the Galactic model at $D = 4.9 \pm 0.7$ kpc. The values in the table are derived from the Bayesian analysis with a Galactic prior and constrained by θ_E and t_E . For the Sun’s motion, we use $(v_R, v_\phi, v_z)_{\text{Sun}} = (-10, 243, 7) \text{ km s}^{-1}$ (for $(R_\odot, z_\odot) = (8160, 25) \text{ pc}$). We combine the two velocities to estimate the proper motion of disk stars. Finally, by applying Equation (16), we can derive the expected source proper motion $\mu_S = \mu_L - \mu_{\text{rel, hel}}$ for a given value of the parallax. Figure 10 shows the results for values of π_E out to the 1σ Spitzer-only contours for the $(u > 0)$ solution (the results for the $(u < 0)$ solution are nearly identical). The properties of bulge stars are derived from Gaia stars within $5'$ of the target: $\mu_{\text{bulge}}(\ell, b) = (-6.310, -0.163) \pm (0.088, 0.076) \text{ mas yr}^{-1}$ and $\sigma_{\text{bulge}}(\ell, b) = (3.176, 2.768) \pm (0.062, 0.054) \text{ mas yr}^{-1}$. To account for the uncertainty in the lens motion, we add the proper-motion dispersions of the disk and bulge in quadrature. One of the two Spitzer minima suggests a source more than 2σ from the bulge distribution, but the other minimum is consistent with a bulge source at $\sim 1.5\sigma$. Therefore, there is no reason to believe that the Spitzer π_E requires a lens proper motion in tension with the motion of typical disk stars.

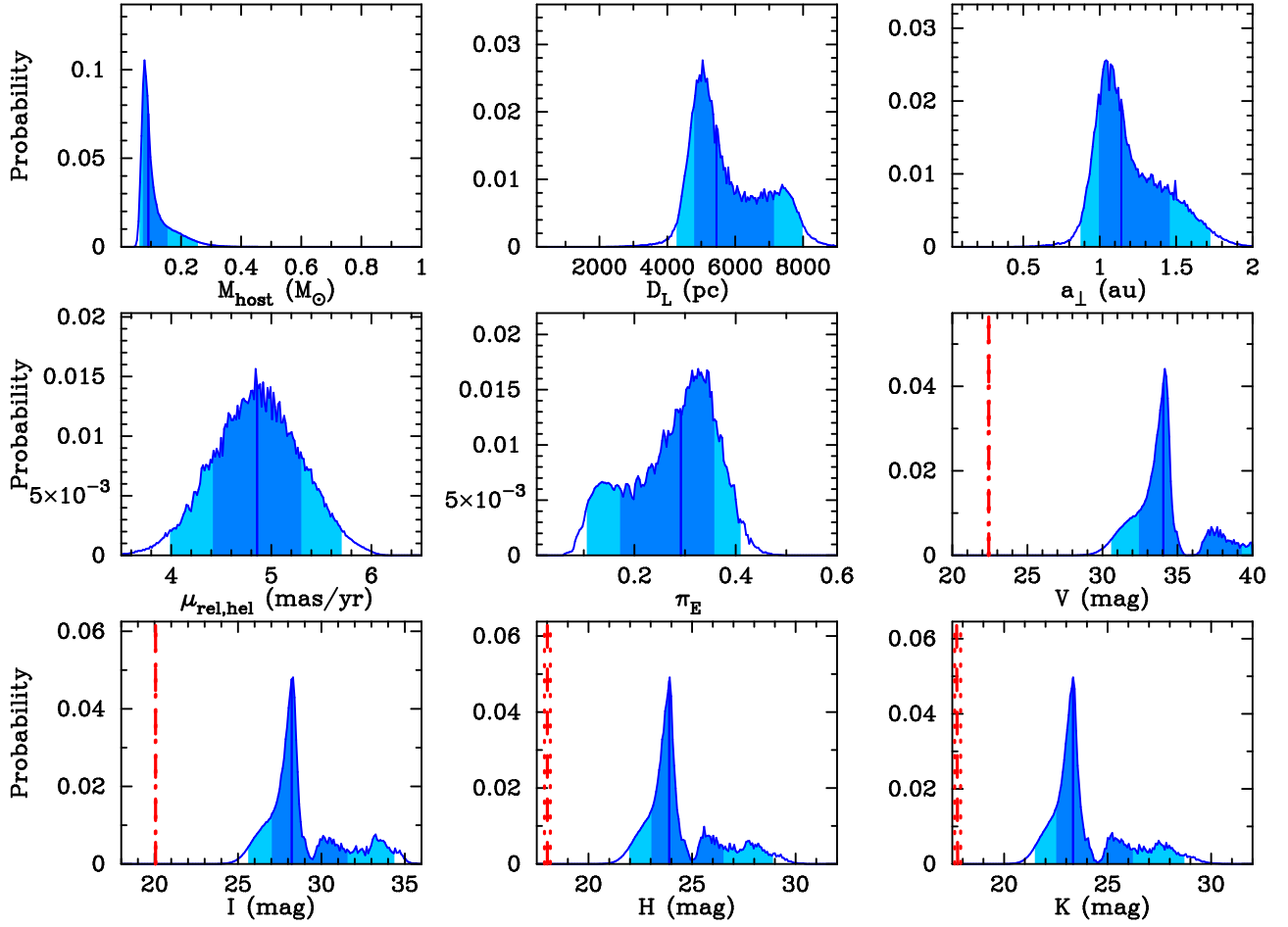


Figure 9. Same as Figure 4, but with the addition of the π_E constraint from the Spitzer-only parallax measurement.

Table 5
Disk Star Velocities and Proper Motions at $D = 4.9 \pm 0.7$ kpc

Star Component	Velocity Component	Unit	-2σ	-1σ	Median	$+1\sigma$	$+2\sigma$
Thin Disk	v_l	km s^{-1}	110.7	163.6	205.9	242.4	280.7
	v_b	km s^{-1}	-95.0	-48.8	-13.7	22.4	71.1
	$\mu_{\text{hel},l}$	mas yr^{-1}	-5.615	-3.349	-1.577	-0.024	1.656
	$\mu_{\text{hel},b}$	mas yr^{-1}	-4.364	-2.388	-0.884	0.653	2.690
Thick Disk	v_l	km s^{-1}	60.7	125.2	181.4	236.5	293.7
	v_b	km s^{-1}	-147.8	-86.4	-12.1	63.3	128.6
	$\mu_{\text{hel},l}$	mas yr^{-1}	-7.662	-4.995	-2.602	-0.275	2.177
	$\mu_{\text{hel},b}$	mas yr^{-1}	-6.577	-3.987	-0.808	2.379	5.102
All	v_l	km s^{-1}	103.6	161.0	204.9	242.2	281.3
	v_b	km s^{-1}	-101.1	-50.5	-13.6	24.4	77.4
	$\mu_{\text{hel},l}$	mas yr^{-1}	-5.878	-3.457	-1.620	-0.034	1.685
	$\mu_{\text{hel},b}$	mas yr^{-1}	-4.611	-2.462	-0.883	0.737	2.960

Finally, in order to include the event in the statistical sample for the study of the Galactic distribution of planets, Zhu et al. (2017) proposed the criteria

$$\sigma(D_{8.3}) < 1.4 \text{ kpc}; \quad D_{8.3} \equiv \frac{\text{kpc}}{\pi_{\text{rel}}/\text{mas} + 1/8.3}. \quad (20)$$

We find $D_{8.3} = 5.15 \pm 0.28$ kpc for the ($u_0 > 0$) case and $D_{8.3} = 5.04 \pm 0.28$ kpc for the ($u_0 < 0$) case by combining the measurement of π_E from the Spitzer-only analysis with the

measurement of θ_E from fitting the ground-based light curve. The small $\sigma(D_{8.3})$ is consistent with the expectation for a high-magnification event as investigated by Gould & Yee (2012), Shin et al. (2018), and Gould (2019). They show that accurate parallax measurements are possible even if there are only a few observations taken by Spitzer when the Earth-based magnification is high ($A_{\oplus} \geq 100$). Therefore, in terms of $\sigma_{D_{8.3}}$ (Zhu et al. 2017), the Spitzer-only parallax suggests that the apparent signal is good enough to include OGLE-2018-BLG-1185Lb in

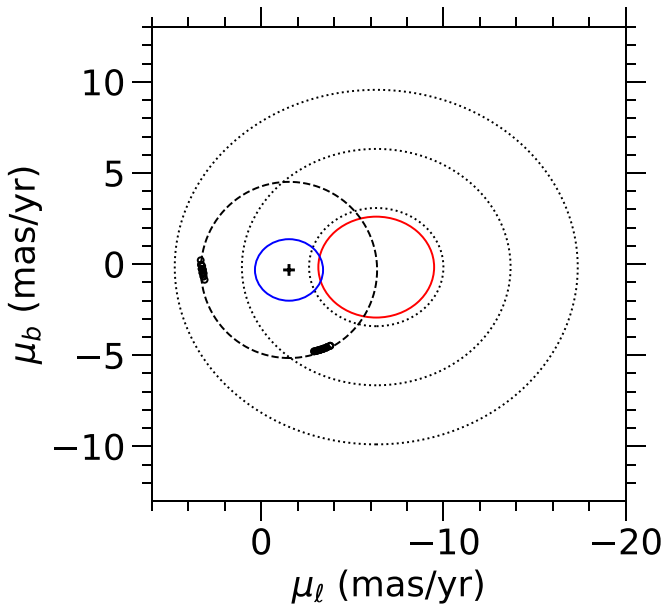


Figure 10. Test of source proper motion predicted by the Spitzer-only parallax. Black points: Derived source proper motions for π_E within 1σ of the minimum for the Spitzer-only contours (based on $\mu_{\text{rel, hel}}$). Black cross: Mean proper motion for disk stars assuming a distance of $D_L = 4.9$ kpc. Dashed circle: Centered on black cross with a radius $\mu_{\text{rel, geo}} = 4.832$ mas yr $^{-1}$. Note that the black cross and dashed circle are merely reference points. Red: 1σ error ellipse for the bulge stars as derived from Gaia. Blue: 1σ error ellipse for the disk stars derived from $(\sigma_{v, \phi}, \sigma_{v, z})$. Black dotted contours: 1σ , 2σ , and 3σ contours adding the dispersions of the bulge and disk in quadrature. The observed constraints are consistent with a lens in the disk and a source in the bulge.

the statistical sample of Spitzer events. However, the systematics need to be studied and understood before membership in the sample can be definitively evaluated.

7. Discussion and Summary

We analyzed the microlensing event OGLE-2018-BLG-1185, which was simultaneously observed from a large number of ground-based telescopes and the Spitzer telescope. The ground-based light-curve modeling indicates a low-mass ratio of $q = (6.9 \pm 0.2) \times 10^{-5}$, which is close to the peak of the wide-orbit exoplanet mass-ratio distribution derived by Suzuki et al. (2016) and investigated further by Udalski et al. (2018) and Jung et al. (2019b). Suzuki et al. (2016) derived the wide-orbit planet occurrence rate using a sample of 30 planets, primarily from the MOA-II microlensing survey during 2007–2012. The planet presented here, OGLE-2018-BLG-1185Lb, will be included in an extension of the MOA-II statistical analysis (Suzuki et al. 2021, in preparation), and its low-mass ratio will help define the mass-ratio function peak.

From the ground-based light-curve modeling, only the finite source effect is detected, yielding a measurement of the angular Einstein radius. However, the physical properties of the lens as derived from the light curve are unclear because the observed flux variation of the Spitzer light curve is marginal. Using only the constraint from the measured angular Einstein radius and a conservative constraint on the change in Spitzer flux, we estimate the host star and planet masses with a Bayesian analysis under the assumption that stars of all masses have an equal probability of hosting the planet. This analysis indicates a host mass of $M_{\text{host}} = 0.37^{+0.35}_{-0.21} M_{\odot}$ and a planet mass of $m_p = 8.4^{+7.9}_{-4.7} M_{\oplus}$ located at $D_L = 7.4^{+0.5}_{-0.9}$ kpc. By contrast, the

Spitzer data favor a larger microlensing parallax, which implies a VLM host with a terrestrial planet ($M_{\text{host}} = 0.091^{+0.064}_{-0.018} M_{\odot}$, $m_p = 2.1^{+1.5}_{-0.4} M_{\oplus}$) that is either in the disk at $D_L \sim 5$ kpc or in the bulge at $D_L \sim 7.5$ kpc (these values include a Galactic prior but are not significantly different from the values without the prior; see Table 4).

Figure 11 compares the Bayesian estimates from the conservative Spitzer flux constraint and the full Spitzer parallax measurement of the host and planet mass for OGLE-2018-BLG-1185 to those of other planetary systems. The pink circles show the microlens planets without mass measurements, and the red circles show the microlens planets with mass measurements from ground-based orbital parallax effects and/or detection of the lens flux by high-resolution follow-up observations. The red squares represent microlens planets with mass measurements from the satellite parallax effect observed by Spitzer. Figure 11 indicates that if the Spitzer parallax is correct, this is one of the lowest-mass planets discovered by microlensing.

However, the result that this is a terrestrial planet orbiting a VLM dwarf in the disk should be treated with caution, because the amplitude of the Spitzer signal is at the level of systematics seen in other events. A comparison of these properties to the Bayesian posteriors (Figure 4) demonstrates that a higher-mass system is preferred given t_E , θ_E , and the Galactic priors. At the same time, a VLM dwarf + terrestrial planet is still within the 2σ range of possibilities from the Bayesian analysis, especially once the constraint on Δf_{Spz} is imposed (Figure 7). Furthermore, Shvartzvald et al. (2017) suggest that such planets might be common. Nevertheless, further investigation is needed in order to assess whether the fitted parallax signal (and so the inferred mass) is real.

Adaptive optics observations are one way to test the Spitzer parallax signal. The Bayesian analysis with ground-based + Δf_{Spz} constraints indicates the lens K -band magnitude with extinction should be $K = 20.8^{+1.8}_{-1.5}$ mag, which is about 3 mag fainter than the source. By contrast, if the Spitzer-only parallax is correct and the lens is a VLM dwarf, it should be $K = 23.3^{+2.9}_{-0.8}$ mag and therefore, much fainter and possibly undetectable. The Bayesian estimate of the heliocentric relative proper motion, $\mu_{\text{rel, hel}} = 5.0 \pm 0.4$ mas yr $^{-1}$, predicts that the angular separation between the source and the lens will be ~ 30 mas around mid-2024. Thus, the lens can be resolved from the source by future follow-up observations with Keck or the Extremely Large Telescope. If such resolved measurements were made (and the lens were luminous), they would also lead to a direct measurement of μ . The observed magnitude of μ can serve as a check on θ_E . Additionally, the direction of μ is the same as the direction of the microlens parallax vector, which could clarify how the Spitzer-only parallax contours should be interpreted in the presence of systematics.

If the Spitzer parallax is verified, this event confirms the potential of microlensing for measuring the wide-orbit planet frequency into the terrestrial planet regime. Although the number of microlens planets with mass measurements is small for now, observing the satellite parallax effect can continue to increase the number. In particular, this effect can be measured for terrestrial planets by simultaneous observations between the ground and L2 (Gould et al. 2003). This can be achieved with the PRIME telescope (principal investigator: Takahiro, Sumi) and the Roman Space Telescope (Spergel et al. 2015; Penny et al. 2019) in the mid-2020s.

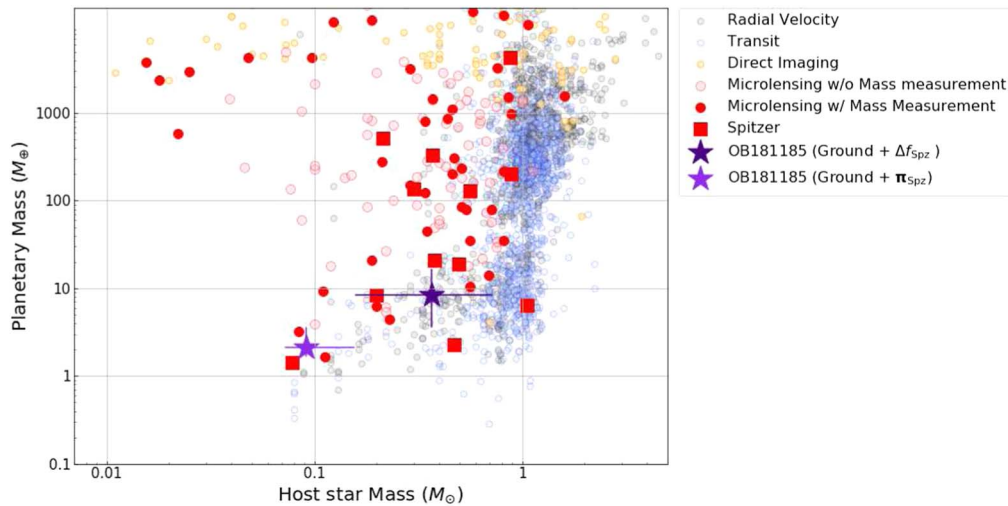


Figure 11. The mass distribution of the detected exoplanets as of 2021 February 25.⁷⁴ The purple stars indicate OGLE-2018-BLG-1185. The pink circles show the microlens planets without mass measurements, and the red circles show the microlens planets with mass measurements from ground-based orbital parallax effects and/or detection of the lens flux by high-resolution follow-up observations. The red squares represent the microlens planets with mass measurements from satellite parallax effects by Spitzer. The blue, yellow, and black dots indicate planets found by the transit, direct imaging, and radial velocity methods, respectively.

Work by I.K. was supported by JSPS KAKENHI grant No. 20J20633. Work by J.C.Y. was supported by Jet Propulsion Laboratory grant 1571564. Work by D.P.B., A.B., and C.R. was supported by NASA through grant NASA-80NSSC18K0274. T.S. acknowledges financial support from the JSPS (JSPS23103002, JSPS24253004, and JSPS26247023). Work by N.K. is supported by JSPS KAKENHI grant No. JP18J00897. A.S. is a University of Auckland doctoral scholar. Y.T. acknowledges the support of DFG priority program SPP 1992 Exploring the Diversity of Extrasolar Planets (WA 1047/11-1). T.C.H. acknowledges financial support from the National Research Foundation (No. 2019R111A1A01059609). U.G.J. acknowledges support from H2020-MSCA-ITN-2019, grant No. 860470 (CHAMELEON), and the NovoNordisk Foundation grant No. NNF19OC0057374. W.Z. and S.M. acknowledge support by the National Science Foundation of China (grant Nos. 11821303 and 11761131004). Work by C.H. was supported by grants of the National Research Foundation of Korea (2020R1A4A2002885 and 2019R1A2C2085965). Funding for B.S.G. was provided by NASA grant NNG16PJ32C and the Thomas Jefferson Chair for Discovery and Space Exploration. The MOA project is supported by JSPS KAKENHI

grant Nos. JSPS24253004, JSPS26247023, JSPS23340064, JSPS15H00781, JP16H06287, 17H02871, and 19KK0082. The OGLE project has received funding from the National Science Centre, Poland, grant MAESTRO 2014/14/A/ST9/00121 to AU. This research has made use of the KMTNet system operated by the Korea Astronomy and Space Science Institute and the data were obtained at the three host sites of CTIO in Chile, SAAO in South Africa, and SSO in Australia. This research uses data obtained through the Telescope Access Program (TAP), which has been funded by the TAP member institutes. This work has made use of data from the European Space Agency mission Gaia (<https://www.cosmos.esa.int/gaia>), processed by the Gaia Data Processing and Analysis Consortium (DPAC; <https://www.cosmos.esa.int/web/gaia/dpac/consortium>). Funding for DPAC has been provided by national

institutions, in particular the institutions participating in the Gaia Multilateral Agreement. This research has made use of the NASA Exoplanet Archive, which is operated by the California Institute of Technology, under contract with the National Aeronautics and Space Administration under the Exoplanet Exploration Program.

Software: OGLE DIA pipeline (Udalski 2003), MOA DIA pipeline (Bond et al. 2001), KMTNet pySIS pipeline (Albrow et al. 2009), DanDIA (Bramich 2008; Bramich et al. 2013), DoPHOT (Schechter et al. 1993), ISIS (Alard & Lupton 1998; Alard 2000; Zang et al. 2018), image-centered ray-shooting method (Bennett & Rhie 1996; Bennett 2010).

Appendix Constraints on the Blended Light and Discrepancy with Gaia

The blended light in this event is roughly four times brighter than the source. In principle, the blend could be the lens itself or a companion to either the lens or the source. If so, it could constrain the flux and proper motion of the lens or the proper motion of the source.

From the KMTNet images, we measure the astrometric offset between the source and the baseline object and find an offset of $0''.175$. This offset is larger than the astrometric uncertainties. Therefore, if it is a companion to the lens or source, it must be a very wide separation companion (~ 1000 au). However, the large separation also suggests that it could be an ambient star unrelated to the microlensing event.

We measure the proper motion of the baseline object based on 10 yr of OGLE survey data and find $\mu_{\text{base}}(\text{R.A., decl.}) = (-6.00 \pm 0.26, -4.25 \pm 0.16) \text{ mas yr}^{-1}$. Because the blend is much brighter than the source, its motion should dominate the measured μ_{base} . The measured value is very consistent with typical proper motions for normal bulge stars, but not unreasonable for the proper motion of a disk star. Hence, it does not rule out the possibility that the blend is a wide-separation companion to the source or the lens, but it also shows that the blend could easily be an unrelated bulge star.





For completeness, we note that the OGLE measurement of the proper motion of the baseline object is inconsistent with

⁷⁴ <http://exoplanetarchive.ipac.caltech.edu>

the reported Gaia proper motion of the nearest Gaia source (4062756831332827136; Gaia Collaboration et al. 2016). Gaia EDR3 (Gaia Collaboration et al. 2021) reports there is a $G = 20.1$ mag star $0''.177$ from the OGLE coordinates for the baseline star (17:59:10.26–27:50:06.3). The reported proper motion of this source is $\mu(\text{R.A., decl.}) = (-12.173 \pm 1.247, -9.714 \pm 0.870) \text{ mas yr}^{-1}$, which is an outlier relative to the typical proper motions for stars in this field. Gaia DR2 (Gaia Collaboration et al. 2018) reports an only slightly less extreme proper motion of $\mu(\text{R.A., decl.}) = (-8.475 \pm 2.234, -4.039 \pm 1.985) \text{ mas yr}^{-1}$. The nature of this discrepancy is unknown, but because the Gaia proper motion is highly unusual (and the OGLE proper motion is typical), and the Gaia measurement varies significantly between DR2 and EDR3, this suggests a problem with the Gaia measurement.

ORCID iDs

Iona Kondo  <https://orcid.org/0000-0002-3401-1029>
 Jennifer C. Yee  <https://orcid.org/0000-0001-9481-7123>
 David P. Bennett  <https://orcid.org/0000-0001-8043-8413>
 Takahiro Sumi  <https://orcid.org/0000-0002-4035-5012>
 Naoki Koshimoto  <https://orcid.org/0000-0003-2302-9562>
 Andrzej Udalski  <https://orcid.org/0000-0001-5207-5619>
 Yossi Shvartzvald  <https://orcid.org/0000-0003-1525-5041>
 Youn Kil Jung  <https://orcid.org/0000-0002-0314-6000>
 Weicheng Zang  <https://orcid.org/0000-0001-6000-3463>
 Valerio Bozza  <https://orcid.org/0000-0003-4590-0136>
 Etienne Bachelet  <https://orcid.org/0000-0002-6578-5078>
 Nicholas J. Rattenbury  <https://orcid.org/0000-0001-5069-319X>
 R. Barry  <https://orcid.org/0000-0003-4916-0892>
 A. Fukui  <https://orcid.org/0000-0002-4909-5763>
 Y. Itow  <https://orcid.org/0000-0002-8198-1968>
 S. Miyazaki  <https://orcid.org/0000-0001-9818-1513>
 Y. Muraki  <https://orcid.org/0000-0003-1978-2092>
 G. Olmschenk  <https://orcid.org/0000-0001-8472-2219>
 C. Ranc  <https://orcid.org/0000-0003-2388-4534>
 P. Mróz  <https://orcid.org/0000-0001-7016-1692>
 R. Poleski  <https://orcid.org/0000-0002-9245-6368>
 J. Skowron  <https://orcid.org/0000-0002-2335-1730>
 M. K. Szymański  <https://orcid.org/0000-0002-0548-8995>
 I. Soszyński  <https://orcid.org/0000-0002-7777-0842>
 S. Kozłowski  <https://orcid.org/0000-0003-4084-880X>
 P. Pietrukowicz  <https://orcid.org/0000-0002-2339-5899>
 K. Ulaczyk  <https://orcid.org/0000-0001-6364-408X>
 P. Iwanek  <https://orcid.org/0000-0002-6212-7221>
 M. D. Albrow  <https://orcid.org/0000-0003-3316-4012>
 C. Han  <https://orcid.org/0000-0002-2641-9964>
 K.-H. Hwang  <https://orcid.org/0000-0002-9241-4117>
 I.-G. Shin  <https://orcid.org/0000-0002-4355-9838>
 G. Bryden  <https://orcid.org/0000-0001-5966-837X>
 S. Carey  <https://orcid.org/0000-0002-0221-6871>
 B. S. Gaudi  <https://orcid.org/0000-0003-0395-9869>
 C. B. Henderson  <https://orcid.org/0000-0001-8877-9060>
 D. Maoz  <https://orcid.org/0000-0002-6579-0483>
 M. T. Penny  <https://orcid.org/0000-0001-7506-5640>
 U. G. Jørgensen  <https://orcid.org/0000-0001-7303-914X>
 N. Peixinho  <https://orcid.org/0000-0002-6830-476X>
 S. Sajadian  <https://orcid.org/0000-0002-2859-1071>
 C. Snodgrass  <https://orcid.org/0000-0001-9328-2905>
 E. Khalouei  <https://orcid.org/0000-0001-5098-4165>
 S. Rahvar  <https://orcid.org/0000-0002-7084-5725>

M. Rabus  <https://orcid.org/0000-0003-2935-7196>
 R. A. Street  <https://orcid.org/0000-0001-6279-0552>
 K. Horne  <https://orcid.org/0000-0003-1728-0304>
 J. Wambsganss  <https://orcid.org/0000-0002-8365-7619>
 A. Saha  <https://orcid.org/0000-0002-6839-4881>

References

- Alard, C. 2000, *A&AS*, **144**, 363
 Alard, C., & Lupton, R. H. 1998, *ApJ*, **503**, 325
 Albrow, M. D., Horne, K., Bramich, D. M., et al. 2009, *MNRAS*, **397**, 2099
 Baraffe, I., Chabrier, G., Barman, T. S., Allard, F., & Hauschildt, P. H. 2003, *A&A*, **402**, 701
 Batista, V., Beaulieu, J.-P., Bennett, D. P., et al. 2015, *ApJ*, **808**, 170
 Batista, V., Beaulieu, J.-P., Gould, A., et al. 2014, *ApJ*, **780**, 54
 Bennett, D. P. 2010, *ApJ*, **716**, 1408
 Bennett, D. P., Anderson, J., Bond, I. A., Udalski, A., & Gould, A. 2006, *ApJL*, **647**, L171
 Bennett, D. P., Anderson, J., & Gaudi, B. S. 2007, *ApJ*, **660**, 781
 Bennett, D. P., Bhattacharya, A., Anderson, J., et al. 2015, *ApJ*, **808**, 169
 Bennett, D. P., Bhattacharya, A., Beaulieu, J.-P., et al. 2020, *AJ*, **159**, 68
 Bennett, D. P., Bond, I. A., Udalski, A., et al. 2008, *ApJ*, **684**, 663
 Bennett, D. P., & Rhie, S. H. 1996, *ApJ*, **472**, 660
 Bensby, T., Yee, J. C., Feltzing, S., et al. 2013, *A&A*, **549**, A147
 Bhattacharya, A., Beaulieu, J.-P., Bennett, D. P., et al. 2018, *AJ*, **156**, 289
 Bhattacharya, A., Bennett, D. P., Anderson, J., et al. 2017, *AJ*, **154**, 59
 Bond, I. A., Abe, F., Dodd, R. J., et al. 2001, *MNRAS*, **327**, 868
 Bond, I. A., Bennett, D. P., Sumi, T., et al. 2017, *MNRAS*, **469**, 2434
 Boyajian, T. S., van Belle, G., & von Braun, K. 2014, *AJ*, **147**, 47
 Bramich, D. M. 2008, *MNRAS*, **386**, L77
 Bramich, D. M., Horne, K., Albrow, M. D., et al. 2013, *MNRAS*, **428**, 2275
 Brown, T. M., Baliber, N., Bianco, F. B., et al. 2013, *PASP*, **125**, 1031
 Calchi Novati, S., Gould, A., Yee, J. C., et al. 2015, *ApJ*, **814**, 92
 Calchi Novati, S., Skowron, J., Jung, Y. K., et al. 2018, *AJ*, **155**, 261
 Calchi Novati, S., Suzuki, D., Udalski, A., et al. 2019, *AJ*, **157**, 121
 Cardelli, J. A., Clayton, G. C., & Mathis, J. S. 1989, *ApJ*, **345**, 245
 Cassan, A., Kubas, D., Beaulieu, J.-P., et al. 2012, *Natur*, **481**, 167
 Chung, S.-J., Han, C., Park, B.-G., et al. 2005, *ApJ*, **630**, 535
 Claret, A., & Bloemen, S. 2011, *A&A*, **529**, A75
 Dominik, M. 1999, *A&A*, **349**, 108
 Fukui, A., Gould, A., Sumi, T., et al. 2015, *ApJ*, **809**, 74
 Fukui, A., Suzuki, D., Koshimoto, N., et al. 2019, *AJ*, **158**, 206
 Gaia Collaboration, Brown, A. G. A., Vallenari, A., et al. 2018, *A&A*, **616**, A1
 Gaia Collaboration, Brown, A. G. A., Vallenari, A., et al. 2021, *A&A*, **650**, C3
 Gaia Collaboration, Prusti, T., de Bruijne, J. H. J., et al. 2016, *A&A*, **595**, A1
 Gaudi, B. S. 1998, *ApJ*, **506**, 533
 González Hernández, J. I., & Bonifacio, P. 2009, *A&A*, **497**, 497
 Gould, A. 1992, *ApJ*, **392**, 442
 Gould, A. 1994, *ApJL*, **421**, L71
 Gould, A. 2000, *ApJ*, **542**, 785
 Gould, A. 2004, *ApJ*, **606**, 319
 Gould, A. 2019, *JKAS*, **52**, 121
 Gould, A., Carey, S., & Yee, J. 2014, sptz prop, 11006
 Gould, A., Carey, S., & Yee, J. 2016, sptz prop, 13005
 Gould, A., Dong, S., Gaudi, B. S., et al. 2010, *ApJ*, **720**, 1073
 Gould, A., Gaudi, B. S., & Han, C. 2003, *ApJL*, **591**, L53
 Gould, A., & Loeb, A. 1992, *ApJ*, **396**, 104
 Gould, A., Ryu, Y.-H., Calchi Novati, S., et al. 2020, *JKAS*, **53**, 9
 Gould, A., Udalski, A., An, D., et al. 2006, *ApJL*, **644**, L37
 Gould, A., Yee, J., & Carey, S. 2015a, sptz prop, 12013
 Gould, A., Yee, J., & Carey, S. 2015b, sptz prop, 12015
 Gould, A., Yee, J., Carey, S., et al. 2018, sptz prop, 14012
 Gould, A., & Yee, J. C. 2012, *ApJL*, **755**, L17
 Gould, A., & Yee, J. C. 2013, *ApJ*, **764**, 107
 Griest, K., & Hu, W. 1993, *ApJ*, **407**, 440
 Griest, K., & Safizadeh, N. 1998, *ApJ*, **500**, 37
 Hirao, Y., Bennett, D. P., Ryu, Y.-H., et al. 2020, *AJ*, **160**, 74
 Holtzman, J. A., Watson, A. M., Baum, W. A., et al. 1998, *AJ*, **115**, 1946
 Ida, S., & Lin, D. N. C. 2004, *ApJ*, **604**, 388
 Jung, Y. K., Gould, A., Udalski, A., et al. 2019, *AJ*, **158**, 28
 Jung, Y. K., Gould, A., Zang, W., et al. 2019b, *AJ*, **157**, 72
 Kenyon, S. J., & Hartmann, L. 1995, *ApJS*, **101**, 117
 Kim, D. J., Kim, H. W., Hwang, K. H., et al. 2018, *AJ*, **155**, 76
 Kim, S.-L., Lee, C.-U., Park, B.-G., et al. 2016, *JKAS*, **49**, 37
 Kondo, I., Sumi, T., Bennett, D. P., et al. 2019, *AJ*, **158**, 224

- Koshimoto, N., Baba, J., & Bennett, D. P. 2021a, arXiv:2104.03306
- Koshimoto, N., & Bennett, D. P. 2020, *AJ*, **160**, 177
- Koshimoto, N., & Ranc, C. 2021b, nkoshimoto/genulens: A Tool for Gravitational Microlensing Events Simulation, Zenodo, doi:10.5281/zenodo.4784949
- Koshimoto, N., Shvartzvald, Y., Bennett, D. P., et al. 2017, *AJ*, **154**, 3
- Lambrechts, M., Lega, E., Nelson, R. P., et al. 2019, *A&A*, **630**, A82
- Lissauer, J. J. 1993, *ARA&A*, **31**, 129
- Nataf, D. M., Gould, A., Fouqué, P., et al. 2013, *ApJ*, **769**, 88
- Nayakshin, S., Dipierro, G., & Szulágyi, J. 2019, *MNRAS*, **488**, L12
- Nucita, A. A., Licchelli, D., De Paolis, F., et al. 2018, *MNRAS*, **476**, 2962
- Penny, M. T., Gaudi, B. S., Kerins, E., et al. 2019, *ApJS*, **241**, 3
- Poleski, R., Zhu, W., Christie, G. W., et al. 2016, *ApJ*, **823**, 63
- Pollack, J. B., Hubickyj, O., Bodenheimer, P., et al. 1996, *Icar*, **124**, 62
- Refsdal, S. 1966, *MNRAS*, **134**, 315
- Ryu, Y.-H., Yee, J. C., Udalski, A., et al. 2018, *AJ*, **155**, 40
- Sako, T., Sekiguchi, T., Sasaki, M., et al. 2008, *ExA*, **22**, 51
- Schechter, P. L., Mateo, M., & Saha, A. 1993, *PASP*, **105**, 1342
- Shan, Y., Yee, J. C., Udalski, A., et al. 2019, *ApJ*, **873**, 30
- Sharma, S., Bland-Hawthorn, J., Binney, J., et al. 2014, *ApJ*, **793**, 51
- Shin, I.-G., Udalski, A., Yee, J. C., et al. 2018, *ApJ*, **863**, 23
- Shvartzvald, Y., Yee, J. C., Calchi Novati, S., et al. 2017, *ApJL*, **840**, L3
- Spergel, D., Gehrels, N., Baltay, C., et al. 2015, arXiv:1503.03757
- Street, R. A., Udalski, A., Calchi Novati, S., et al. 2016, *ApJ*, **819**, 93
- Sumi, T., Abe, F., Bond, I. A., et al. 2003, *ApJ*, **591**, 204
- Sumi, T., Bennett, D. P., Bond, I. A., et al. 2010, *ApJ*, **710**, 1641
- Suzuki, D., Bennett, D. P., Ida, S., et al. 2018, *ApJL*, **869**, L34
- Suzuki, D., Bennett, D. P., Sumi, T., et al. 2016, *ApJ*, **833**, 145
- Tsapras, Y., Street, R. A., Hundertmark, M., et al. 2019, *PASP*, **131**, 124401
- Udalski, A. 2003, *AcA*, **53**, 291
- Udalski, A., Ryu, Y.-H., Sajadian, S., et al. 2018, *AcA*, **68**, 1
- Udalski, A., Szymanski, M., Kaluzny, J., et al. 1994, *AcA*, **44**, 227
- Udalski, A., Szymański, M. K., & Szymański, G. 2015, *AcA*, **65**, 1
- Udalski, A., Yee, J. C., Gould, A., et al. 2015, *ApJ*, **799**, 237
- Vandorou, A., Bennett, D. P., Beaulieu, J.-P., et al. 2020, *AJ*, **160**, 121
- Verde, L., Peiris, H. V., Spergel, D. N., et al. 2003, *ApJS*, **148**, 195
- Yee, J. C., Gould, A., Beichman, C., et al. 2015, *ApJ*, **810**, 155
- Yee, J. C., Zang, W., Udalski, A., et al. 2021, arXiv:2101.04696
- Yoo, J., DePoy, D. L., Gal-Yam, A., et al. 2004, *ApJ*, **603**, 139
- Zang, W., Dong, S., Gould, A., et al. 2020, *ApJ*, **897**, 180
- Zang, W., Penny, M. T., Zhu, W., et al. 2018, *PASP*, **130**, 104401
- Zang, W., Shvartzvald, Y., Udalski, A., et al. 2020, arXiv:2010.08732
- Zang, W., Shvartzvald, Y., Wang, T., et al. 2020, *ApJ*, **891**, 3
- Zhu, W., Udalski, A., Novati, S. C., et al. 2017, *AJ*, **154**, 210